

# Dynamical suppression of fluctuations in an interacting nuclear spin bath of a self-assembled quantum dot using multiple pulse nuclear magnetic resonance

A. M. Waeber\*

*Department of Physics and Astronomy, University of Sheffield, Sheffield S3 7RH, United Kingdom and  
Walter Schottky Institut and Physik-Department,  
Technische Universität München, Am Coulombwall 4, 85748 Garching, Germany*

M. Hopkinson

*Department of Electronic and Electrical Engineering,  
University of Sheffield, Sheffield S1 3JD, United Kingdom*

M. S. Skolnick and E. A. Chekhovich<sup>†</sup>

*Department of Physics and Astronomy, University of Sheffield, Sheffield S3 7RH, United Kingdom*

(Dated: March 8, 2024)

Electron spin qubit coherence in quantum dots is ultimately limited by random nuclear spin bath fluctuations. Here we aim to eliminate this randomness by making spin bath evolution deterministic. We introduce spin bath control sequences, which systematically combine Hahn and solid echoes to suppress inhomogeneous broadening and nuclear-nuclear interactions. Experiments on self-assembled quantum dots show a five-fold increase in nuclear spin coherence. Numerical simulations show that these sequences can be used to suppress decoherence via qubit-qubit interaction in point defect and dopant spin systems.

The excellent spin-photon interface of confined charges in III-V semiconductor quantum dots (QDs) has recently attracted a lot of attention for potential applications in photon-mediated quantum networks<sup>1–3</sup>. The large optical dipole moment of QDs makes ultrafast optical spin control feasible and permits unrivalled entanglement generation rates<sup>4–6</sup>. On the other hand, the coherence properties of the electron or hole spin qubit are strongly affected by hyperfine interaction with the fluctuating spin bath of the  $\sim 10^5$  constituent nuclei of the QD<sup>7,8</sup>.

Recently, significant progress has been made in suppressing hyperfine-induced qubit dephasing in strain-free QDs by applying tailored dynamical decoupling protocols to the qubit spin<sup>9,10</sup>. However, there are limits to this approach: in a strained QD, static quadrupolar fields lead to a spread of the nuclear spin Larmor frequencies, reducing the effectiveness of such a spectral filtering method<sup>11–14</sup>.

In order to improve the properties of the qubit environment directly, we explore the complementary pathway of controlling the nuclear spin bath itself with pulsed nuclear magnetic resonance (NMR)<sup>15,16</sup>. Examples for controlling spin-spin interactions are found in NMR spectroscopy where sequences such as WAHUHA<sup>17</sup> and MREV<sup>18,19</sup> are used to average out dipolar couplings selectively. However, these ‘solid echo’ cycles do not refocus inhomogeneous broadening caused by additional static or time-dependent fields. On the other hand, dynamical decoupling sequences consisting of a series of  $\pi$ -pulses can suppress this inhomogeneous dephasing very effectively<sup>20–22</sup>, but are unsuitable for controlling dipolar coupling terms. Instead, such sequences even increase dipolar dephasing through the parasitic effect of instantaneous diffusion<sup>23–25</sup>.

In this work, we introduce a set of pulse sequences which are designed to combine the features of dynamical decoupling with those of solid echoes. Under these *combined Hahn and solid echo* (CHASE) multiple pulse sequences, we engineer the dynamics of the interacting many-body nuclear spin bath in a single InGaAs QD. While it is not possible to eliminate spin bath dynamics completely, we show that random fluctuations can be transformed into deterministic evolution, which can in principle be decoupled from the qubit using standard control schemes<sup>16</sup>. We test CHASE sequences experimentally in optically detected nuclear magnetic resonance (ODNMR) measurements and explore their applicability to systems with and without strong inhomogeneous resonance broadening using first principle quantum mechanical simulations. Our experimental results reveal an up to fivefold increase in the CHASE nuclear spin coherence time of  $^{75}\text{As}$  compared to the Hahn echo<sup>26</sup>. Furthermore, our simulations show that cyclic application of CHASE sequences can suppress dephasing arbitrarily well in spin ensembles with weak inhomogeneous broadening (e.g. strain-free quantum dots, dilute donor spins or defect centres).

Before presenting experimental results, we describe how the control sequences are designed.

We start from an intuitive approach previously used to extend nuclear spin lifetimes in silicon and diamond<sup>27,28</sup>: by combining solid echo cycles with refocusing  $\pi$ -pulses, both inhomogeneous dephasing and dipolar coupling can be suppressed. Here we substantiate this approach by applying a rigorous average Hamiltonian theory (AHT)<sup>29</sup>, which is a form of perturbation theory based on Magnus expansion. The evolution of a spin-1/2 nuclear bath  $I_i$  is analysed under a given pulse cycle in an external magnetic field  $B_z$ . We take into account a dipolar coupling term  $\mathcal{H}_d^{zz}$  as well as a generic resonance offset Hamiltonian  $\mathcal{H}_0^z$ , which describes inhomogeneous resonance broadening caused for example by chemical shifts or by a static quadrupolar interaction:

$$\begin{aligned} \mathcal{H} &= \mathcal{H}_0^z + \mathcal{H}_d^{zz} \\ &= h \sum_i \Delta\nu_i I_{z,i} + h \sum_{i<j} \nu_{ij} (3I_{z,i}I_{z,j} - \mathbf{I}_i \cdot \mathbf{I}_j) , \end{aligned} \quad (1)$$

where  $\Delta\nu_i$  denotes the resonance frequency offset of the  $i$ -th nuclear spin and  $\nu_{ij}$  is the dipolar coupling constant between two spins  $I_i$  and  $I_j$ . The free decay of transverse magnetisation under this Hamiltonian is described by a rate  $\Gamma \propto 1/T_2^*$ .

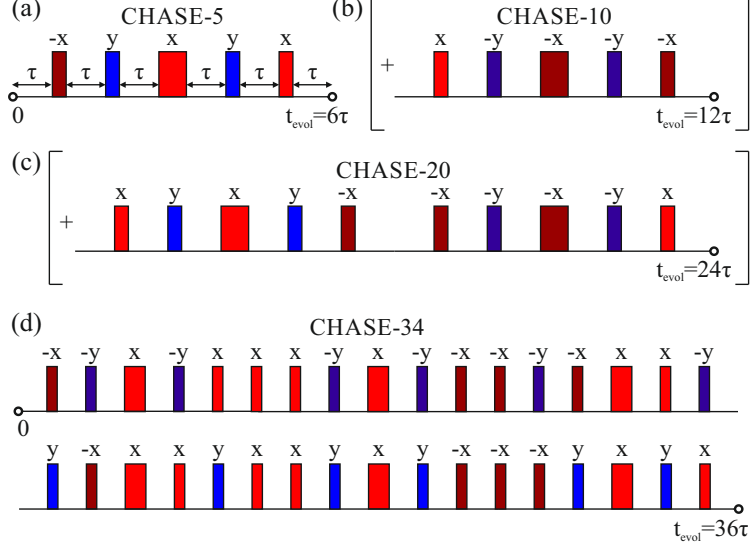


FIG. 1. Pulse sequences for refocusing inhomogeneous and dipolar broadening. The rf carrier phases are  $\varphi_x = 0$ ,  $\varphi_{-x} = \pi$  for  $\pm x$  rotations around the  $\hat{e}_x$  axis, and  $\varphi_y = \pi/2$ ,  $\varphi_{-y} = 3\pi/2$  for  $\pm y$  rotations around  $\hat{e}_y$ . Narrow pulses indicate  $\pi/2$ -rotations with pulse time  $t_\pi/2$  and broad pulses correspondingly represent  $\pi$ -rotations with duration  $t_\pi$ . (a) The combined Hahn and solid echo sequence CHASE-5 with cycle time  $t_c = 3t_\pi + \tau_{\text{evol}}$  consisting of the total gate time  $3t_\pi$  and total free evolution time  $\tau_{\text{evol}} = 6\tau$  (where  $\tau \gg t_\pi$  is the free evolution time between two pulses). (b) Extension to CHASE-10, which is less sensitive to finite pulse durations  $t_\pi > 0$ . (c) Using symmetry considerations, a further optimised sequence CHASE-20 is constructed. (d) The longest sequence CHASE-34 has the best refocusing capability for  $t_\pi \rightarrow 0$ .

Using AHT as a benchmark tool (see details in Supplemental Material<sup>32</sup>) we have analysed various combinations of  $\pi$  and  $\pi/2$  pulses to find those that maximise the spin bath coherence while minimising the pulse sequence length. The shortest efficient cycle which gives a noticeable increase of bath coherence (CHASE-5) contains only 5 pulses and is illustrated in Fig. 1(a). Assuming infinitely short pulses ( $t_\pi \rightarrow 0$ ), the zeroth order average Hamiltonian  $\propto \Gamma$  vanishes. The leading residual contribution to dephasing is a first order term  $\propto \hbar t_c \Gamma^2$  mixing contributions from the inhomogeneous broadening Hamiltonian and the dipolar interaction<sup>30,31</sup>:

$$\bar{\mathcal{H}}_{\text{CHASE-5}} = \frac{it_c}{18\hbar} [\mathcal{H}_d^{zz} - \mathcal{H}_d^{xx}, \mathcal{H}_0^y] + \mathcal{O}(\hbar t_c^2 \Gamma^3), \quad (2)$$

where  $t_c$  is the full cycle time and  $\mathcal{H}_d^{xx}$ ,  $\mathcal{H}_0^y$  are the dipolar and inhomogeneous broadening Hamiltonians acting along orthogonal equatorial axes  $\hat{e}_x$  and  $\hat{e}_y$  (see Supplemental Material<sup>32</sup> for the full definition).

Under realistic experimental conditions, the assumption of infinitely short pulses is often not justified. For finite pulse durations  $t_\pi$ , the zeroth order average Hamiltonian does not vanish under CHASE-5, reducing the capability of the cycle to increase the spin bath coherence. However, we can obtain an average Hamiltonian of the form of Eq. 2 even for finite  $t_\pi$  by extending our cycle to CHASE-10 as illustrated in Fig. 1(b), analogous to the pure solid echo extension from WAHUA to MREV<sup>18,19</sup>. Furthermore, by adding the pulse block shown in Fig. 1(c) we can symmetrise the cycle to CHASE-20 and remove the first-order mixing term, condensing the average Hamiltonian to  $\bar{\mathcal{H}}_{\text{CHASE-20}} \propto \mathcal{O}(\hbar t_c^2 \Gamma^3)$  independent of the pulse duration  $t_\pi$ .

Finally, we identify a longer sequence CHASE-34 (see Fig. 1(d)) with a total gate time  $20t_\pi$  which reduces the average Hamiltonian to a second order mixing term for  $t_\pi \rightarrow 0$  but has non-vanishing lower-order terms for finite pulse durations. A comprehensive overview of the AHT calculations and residual Hamiltonians for the sequences shown in figure 1 can be found in the Supplemental Material<sup>32</sup>.

We study the performance of these sequences experimentally on individual charge-free InGaAs QDs with  $\sim 10^5$  nuclear spins. Here, we follow the ODNMR pump-probe scheme used in Ref.<sup>26</sup>: the QD sample is kept at  $T = 4.2$  K and is subjected to a strong magnetic field of  $B_z = 8$  T. Using a confocal microscopy setup in Faraday orientation, we prepare the nuclear spin bath optically through polarisation-selective pumping of an exciton transition (dynamic nuclear polarisation, DNP). In this way, we can achieve hyperfine-mediated spin bath polarisation degrees of up to 65%<sup>33,34</sup>. Radio frequency (rf) fields are coupled to the QD via a multi-winding copper coil in close proximity to the sample. Changes in the final bath polarisation are probed with a weak

optical pulse measuring the splitting of the neutral exciton Zeeman doublet<sup>11</sup>.

We perform resonant pulsed NMR measurements on the inhomogeneously broadened central spin transition  $-1/2 \leftrightarrow +1/2$  of the  $^{75}\text{As}$  (inhomogeneous width of  $\Delta\nu_{\text{inh}} \sim 40$  kHz) and  $^{71}\text{Ga}$  ( $\Delta\nu_{\text{inh}} \sim 10$  kHz) nuclear spin ensembles<sup>11,26</sup>. The phases of the  $\pi$ -pulses of all sequences are chosen to produce spin rotations around the  $\hat{e}_x$  axis of the rotating frame. In each experiment, a  $\pi/2$ -pulse is applied prior to the multipulse cycle to initialise the spin state. We conduct experiments with initial  $\pi/2$  rotation around the  $\hat{e}_x$  axis (Carr-Purcell or CP-like sequences<sup>35</sup>, denoted as ‘-X’) and around the  $\hat{e}_y$  axis (Carr-Purcell-Meiboom-Gill or CPMG-like sequences<sup>36</sup>, ‘-Y’): in this way we distinguish between a genuine improvement of the spin coherence and spin locking effects<sup>37–39</sup>, which only stabilize spin magnetization along a certain direction. A final  $\pi/2$ -pulse is an inverse of the initialisation pulse and projects the refocused magnetisation along the  $\hat{e}_z$  axis for optical readout<sup>26</sup>.

Representative data for experiments on  $^{75}\text{As}$  and  $^{71}\text{Ga}$  is shown by the solid symbols in Figs 2(a) and 2(b), respectively. The values of the nuclear spin coherence times  $T_2$  and echo amplitudes  $\Delta E_{\text{hf}}(\tau_{\text{evol}} = 0)$  in Figs 2(c-f) are obtained by fitting the data with a compressed exponential decay function

$$\Delta E_{\text{hf}}(\tau_{\text{evol}}) = \Delta E_{\text{hf}}(\tau_{\text{evol}} = 0) \cdot e^{-(\tau_{\text{evol}}/T_2)^\beta}, \quad (3)$$

where  $\Delta E_{\text{hf}}$  denotes the change in the measured hyperfine shift due to rf-induced depolarisation of the nuclear spin bath,  $\tau_{\text{evol}}$  is the total free evolution time over  $n$  pulse cycles,  $\beta \in [1, 2]$  is a compression factor<sup>40</sup>,  $T_2$  describes decoherence of the spin bath during free evolution, while reduction of the echo amplitude  $\Delta E_{\text{hf}}(\tau_{\text{evol}} = 0)$  compared to the initial magnetization  $\Delta E_{\text{hf}}(t = 0)$  quantifies the imperfections of pulse spin rotations.

In order to analyse the influence of spin locking effects<sup>37–39</sup>, we test a series of CP-X and CP(MG)-Y sequences with alternating pulse carrier phase (sequence cycle  $-\tau/2 - \pi_x - \tau - \pi_{-x} - \tau/2 -$ ). With increasing number of cycles  $n$ , expressed in terms of the total rf gate time, we observe a strong increase of the measured  $T_2$  under CP-X for both isotopes (black squares in Figs 2(c,d)). By contrast, no significant increase of  $T_2$  is observed under CP-Y (blue circles). However, the CP-Y echo amplitude is rapidly reduced with increasing  $n$  (Figs 2(e,f)), owing to the limited available rf power resulting in violation of the ‘hard pulse’ condition<sup>32</sup>.

The contrasting behaviour of  $T_2$  under alternating phase CP-X/Y has been observed in other systems<sup>38,39,41</sup> and has been attributed variably to spin locking<sup>41,42</sup> or stimulated echoes<sup>43</sup>. Here, we ascribe the up-to-fourfold increase of  $T_2$  under CP-X to a form of pulsed spin locking arising

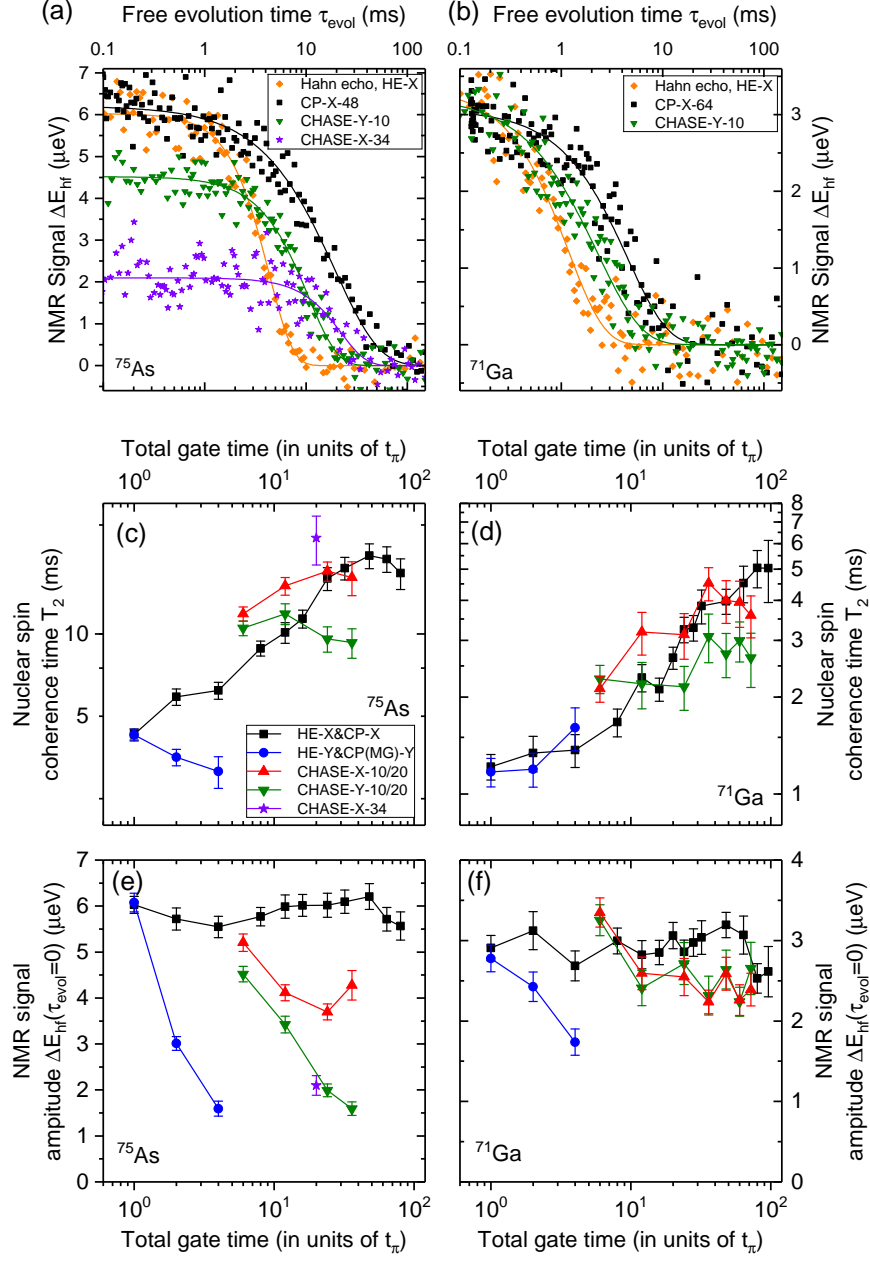


FIG. 2. Nuclear spin polarisation decay under pulsed control of the  $^{75}\text{As}$  and  $^{71}\text{Ga}$  spin ensembles in a single InGaAs QD. (a,b) Decay of the polarisation  $\Delta E_{\text{hf}}$  as a function of the total free evolution time  $\tau_{\text{evol}}$  for different control sequences. Symbols mark experimental data and solid lines show best fits with Eq. 3. (c,d) Dependence of the fitted nuclear spin coherence time  $T_2$  on the number of sequence cycles  $n$  expressed as total rf gate time (in units of the  $\pi$ -pulse time  $t_\pi$ ). Error bars mark 90% confidence intervals. (e,f) Respective fitted echo amplitude  $\Delta E_{\text{hf}}(\tau_{\text{evol}} = 0)$  as a function of the total gate time. The data for one cycle of HE and CHASE-10 is combined with the data for integer cycle numbers  $n$  of CP and CHASE-20, respectively.

from dipolar evolution during the finite  $\pi$ -pulse duration<sup>42</sup>: Our interpretation is based on observation that the spin lock disappears for small pulse-to-cycle time ratios  $t_\pi/t_c$  (see Supplemental Material<sup>32</sup>).

We now examine the spin bath coherence under CHASE-10/20 sequences. In order to account for the spin locking effects discussed above we conduct all experiments with both -X and -Y initialization. In experiments on  $^{75}\text{As}$ , a marked increase of  $T_2^{\text{CHASE-Y-10}} = 10.5 \pm 0.7$  ms compared to the Hahn echo decay  $T_2^{\text{HE-X}} = 4.3 \pm 0.2$  ms is observed even under a single cycle of CHASE-Y-10 (green triangles in Fig. 2). We find a similar proportional increase from  $T_2^{\text{HE-X}} = 1.2 \pm 0.1$  ms to  $T_2^{\text{CHASE-Y-10}} = 2.3 \pm 0.2$  ms for  $^{71}\text{Ga}$ . In comparison, the additional coherence gain under CHASE-Y-20 is only marginal. However, as shown in Figs 2(e,f), the preservation of the echo amplitude  $\Delta E_{\text{hf}}(\tau_{\text{evol}} = 0)$  under CHASE-Y-20 is more robust compared to CP-Y. The CHASE-X-10/20 coherence time (red triangles in Figs. 2(c,d)) exceeds the  $T_2$  of CHASE-Y-10/20, suggesting the presence of spin-locking under CHASE-X-10/20. Thus we use CHASE-Y-10/20 to examine the spectral properties of the spin bath dynamics in a dynamical decoupling fashion: We observe no further coherence gain under up to  $n = 6$  cycles of CHASE-Y-20, suggesting that environment noise (e.g. produced by charge fluctuations) is negligible over a broad frequency domain of up to  $\sim 100$  kHz (given by an average inter-pulse delay of  $\sim 10$   $\mu\text{s}$ ), as expected for neutral QDs<sup>20,26</sup>. Recent work has shown, however, that the nuclear spin bath coherence is drastically reduced when the QD is occupied by an electron<sup>44</sup>. We expect that CHASE sequences will be suited to restore the bath coherence, offering a pathway for electron spin manipulation in a quiescent QD environment.

Finally, we present an experiment using CHASE-34 (violet stars in Fig. 2). We find that only the CP-like cycle yields a measurable decay curve for  $^{75}\text{As}$  whereas the  $^{71}\text{Ga}$  echo amplitude  $\Delta E_{\text{hf}}(\tau_{\text{evol}} = 0)$  is too small to be resolved. Tantalisingly, we observe  $T_2^{\text{CHASE-X-34}} = 22.4 \pm 4.5$  ms (violet stars in Fig. 2(a)) – nearly a fivefold increase of the bath coherence time compared to HE. Numerical simulations (see Supplemental Material<sup>32</sup>) indicate that the reduction of  $\Delta E_{\text{hf}}(\tau_{\text{evol}} = 0)$  in this 34-pulse cycle is not due to the limited rf pulse bandwidth, but is likely related to small pulse calibration errors, offering in principle a route for further improvements.

The experimental observations are corroborated by extensive first principle quantum mechanical simulations of the nuclear spin bath evolution under the studied pulse sequences. We consider an ensemble of twelve dipolar coupled  $^{75}\text{As}$  spins and study the evolution of the resonantly driven central transition in the limits of large ( $\Delta\nu_i \gg \nu_{ij}$ ) and vanishing ( $\Delta\nu_i \ll \nu_{ij}$ ) inhomogeneous broadening. In this way, we can confirm the experimental results in self-assembled QDs with strong static quadrupolar broadening and explore the applicability of CHASE sequences to more

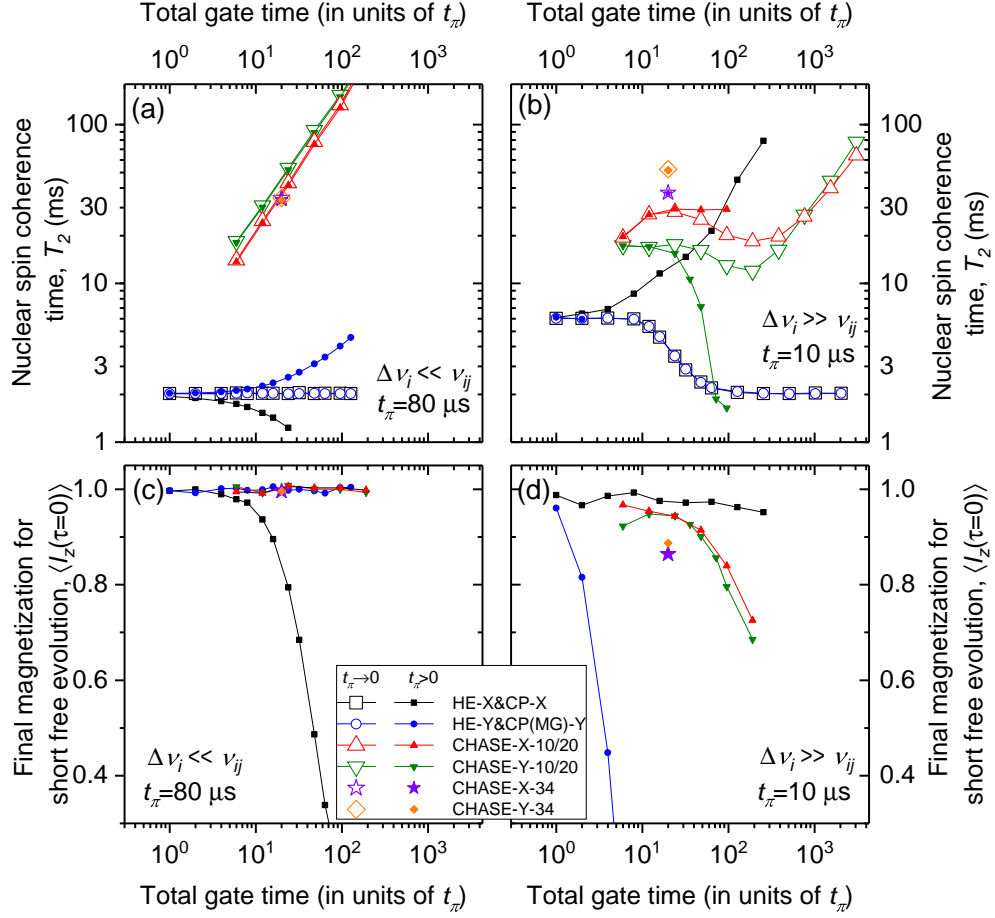


FIG. 3. Simulated evolution of a dipolar coupled ensemble of twelve  $^{75}\text{As}$  spins under control sequences (a,c) with small and (b,d) large inhomogeneous (quadrupolar) broadening  $\Delta\nu_i$ . Figs (a) and (b) show the respective fitted nuclear spin coherence times  $T_2$  as a function of the total gate time. The gate time dependence of the corresponding echo amplitudes for short free evolution  $\langle I_z(0) \rangle$  is shown in (c) and (d). Simulations are done for both infinitely sharp ( $t_\pi = 0$ , open symbols) and finite pulses (solid symbols), where we set  $t_\pi = 80 \mu\text{s}$  for  $\Delta\nu_i \ll \nu_{ij}$  and use  $t_\pi = 10 \mu\text{s}$  in the limit of  $\Delta\nu_i \gg \nu_{ij}$ . Further simulation details and representative decay curves are shown in the Supplemental Material<sup>32</sup>.

homogeneous dilute spin systems as encountered in defect centres in diamond or donors in silicon. In addition, we study the influence of finite pulse durations on the bath evolution by testing our sequences with both infinitely short pulses  $t_\pi \rightarrow 0$  and realistic pulse durations  $t_\pi \sim 10 - 100 \mu\text{s}$ .

Figure 3 shows the fitted coherence times (a,b) and echo amplitudes (c,d) for simulated decay curves in case of negligible inhomogeneous resonance broadening  $\Delta\nu_i \ll \nu_{ij}$  (a,c) and large broadening  $\Delta\nu_i \gg \nu_{ij}$  (b,d). Simulation data at infinitely short (finite) pulses is marked by open



(solid) symbols. The simulations with  $\Delta\nu_i \gg \nu_{ij}$  and finite pulses are in very good agreement with the experiments (cf. Fig. 2(c-f)): namely, the increase in  $T_2$  with increasing number of cycles  $n$  under CP-X (spin locking), the reduction of echo amplitude with growing  $n$  under CP-Y, and the extension of  $T_2$  under CHASE-10/20 are all well reproduced. Moreover, the CHASE-10/20 echo amplitudes are stable under increasing  $n$ , demonstrating the superior performance of CHASE under ‘soft pulse’ conditions compared to previously introduced sequences<sup>28,45,46</sup> (see additional simulations in Supplemental Material<sup>32</sup>).

Having established the validity of the simulations we apply them to the regimes not accessible in experiments on self-assembled QDs. In the case of  $\Delta\nu_i \ll \nu_{ij}$  applicable e.g. to defect spins in diamond and SiC, the effect of the CHASE sequences is analogous to that of a solid echo sequence<sup>17–19</sup>: dipolar broadening can be suppressed arbitrarily well with increasing  $n$  resulting in increase of  $T_2$  (triangles in Fig. 3(a)). Importantly, the CHASE-10/20 echo amplitudes (Fig. 3(c)) remain close to ideal  $\approx 1$  under finite (‘soft’) pulses even at large  $n$ : there is a potential in applying CHASE-10/20 to electron spin qubits for dynamical decoupling from the nuclear spin bath and for simultaneous suppression of the decoherence that arises from qubit-qubit dipolar interactions<sup>15,25</sup> and can not be handled by the standard  $\pi$ -pulse sequences.

Finally, we make a note on some peculiarities predicted in the simulations. For large inhomogeneity ( $\Delta\nu_i \gg \nu_{ij}$ ) and short pulses ( $t_\pi \rightarrow 0$ ) the CP-X/Y coherence time  $T_2$  decreases with increasing  $n$  (open squares and circles in Fig. 3(b)) and asymptotically approaches the  $T_2$  value obtained for weak inhomogeneity ( $\Delta\nu_i \ll \nu_{ij}$ ) (Fig. 3(a)). This is unexpected, since  $\pi$ -pulse trains do not modify the dipolar Hamiltonian. We tentatively ascribe this to fast spin rotations induced by the infinitely short rf pulses: such rotations effectively shorten the spin lifetime, broaden the homogeneous NMR linewidths and re-enable the dipolar nuclear spin flip-flops which are otherwise inhibited by inhomogeneous broadening. Note that similar trends are observed in the simulations with CHASE-10/20 sequences, where the competing effects of the re-enabled flip-flops and convergence of the average Hamiltonian lead to a non-monotonic dependence of  $T_2$  on  $n$ . We also point out that under small inhomogeneous broadening  $\Delta\nu_i \ll \nu_{ij}$  and finite pulse durations, the increase (decrease) of  $T_2$  under CP-Y (CP-X) observed in Fig. 3(a) is reversed compared to the  $\Delta\nu_i \gg \nu_{ij}$  case (Fig. 3(b)) – an unexpected result requiring further investigation.

In summary, we have introduced a set of multiple pulse cycles which allow efficient simultaneous refocusing of inhomogeneous and dipolar broadening. Beyond the current work, these sequences may have potential to restore the spin bath coherence in charged QDs which have recently been shown to possess far shorter Hahn echo decay times<sup>44</sup>. In this way, one would aim to create a

deterministically evolving spin environment for a central electron spin. In addition, CHASE could be used to enhance the coherence of defect centres and dopants beyond the limits of standard dynamical decoupling protocols as the parasitic decoherence channel of instantaneous diffusion<sup>15,25</sup> is quenched. Further optimisation of spin bath fluctuation freezing can be explored using techniques such as optimal control<sup>47</sup>.

The authors are grateful to A. I. Tartakovskii for useful discussions. This work was supported by the EPSRC Programme Grant EP/J007544/1, ITN S<sup>3</sup>NANO. E.A.C. was supported by a University of Sheffield Vice-Chancellor's Fellowship and a Royal Society University Research Fellowship. Computational resources were provided in part by the University of Sheffield HPC cluster Iceberg.

---

\* andreas.waeber@wsi.tum.de

† e.chekhovich@sheffield.ac.uk

- <sup>1</sup> Kimble, H. J. The quantum internet *Nature* **453**, 1023 (2008).
- <sup>2</sup> Akopian, N. and Wang, L. and Rastelli, A. and Schmidt, O. G. and Zwiller, V. Hybrid semiconductor-atomic interface: slowing down single photons from a quantum dot *Nature Photonics* **5**, 230 (2011).
- <sup>3</sup> Meyer, H. M. and Stockill, R. and Steiner, M. and Le Gall, C. and Matthiesen, C. and Clarke, E. and Ludwig, A. and Reichel, J. and Atatüre, M. and Köhl, M. Direct Photonic Coupling of a Semiconductor Quantum Dot and a Trapped Ion *Physical Review Letters* **114**, 123001 (2015).
- <sup>4</sup> Press, D. and Ladd, T. D. and Zhang, B. and Yamamoto, Y. Complete quantum control of a single quantum dot spin using ultrafast optical pulses *Nature* **456**, 218 (2008).
- <sup>5</sup> Delteil, A. and Sun, Z. and Gao, W. and Togan, E. and Faelt, S. and Imamoglu, A. Generation of heralded entanglement between distant hole spins *Nature Physics* **12**, 218 (2016).
- <sup>6</sup> Stockill, R. and Stanley, M. J. and Huthmacher, L. and Clarke, E. and Hugues, M. and Miller, A. J. and Matthiesen, C. and Le Gall, C. and Atatüre, M. Phase-Tuned Entangled State Generation between Distant Spin Qubits *Physical Review Letters* **119**, 010503 (2017).
- <sup>7</sup> Khaetskii, A. V. and Loss, D. and Glazman, L. Electron Spin Decoherence in Quantum Dots due to Interaction with Nuclei *Physical Review Letters* **88**, 186802 (2002).
- <sup>8</sup> Merkulov, I. A. and Efros, A. L. and Rosen, M. Electron spin relaxation by nuclei in semiconductor quantum dots *Physical Review B* **65**, 205309 (2002).
- <sup>9</sup> Bluhm, H. and Foletti, S. and Neder, I. and Rudner, M. and Mahalu, D. and Umansky, V. and Yacoby, A. Dephasing time of GaAs electron-spin qubits coupled to a nuclear bath exceeding 200  $\mu$ s *Nature Physics* **7**, 109 (2011).
- <sup>10</sup> Malinowski, F. K. and Martins, F. and Nissen, P. D. and Barnes, E. and Cywinski, L. and Rudner, M. S. and Fallahi, S. and Gardner, G. C. and Manfra, M. J. and Marcus, C. M. and Kuemmeth, F. Notch

- filtering the nuclear environment of a spin qubit *Nature Nanotechnology* **12**, 16 (2017).
- <sup>11</sup> Chekhovich, E. A. and Kavokin, K. V. and Puebla, J. and Krysa, A. B. and Hopkinson, M. and Andreev, A. D. and Sanchez, A. M. and Beanland, R. and Skolnick, M. S. and Tartakovskii, A. I. Structural analysis of strained quantum dots using nuclear magnetic resonance *Nature Nanotechnology* **7**, 646 (2012).
  - <sup>12</sup> Bechtold, A. and Rauch, D. and Li, F. and Simmet, T. and Ardel, P.-L. and Regler, A. and Müller, K. and Sinitsyn, N. A. and Finley, J. J. Three-stage decoherence dynamics of electron spin qubits in an optically active quantum dot *Nature Physics* **11**, 1005 (2015).
  - <sup>13</sup> Stockill, R. and Le Gall, C. and Matthiesen, C. and Huthmacher, L. and Clarke, E. and Hugues, M. and Atature, M. Quantum dot spin coherence governed by a strained nuclear environment *Nature Communications* **7**, 12745 (2016).
  - <sup>14</sup> Waeber, A. M. and Hopkinson, M. and Farrer, I. and Ritchie, D. A. and Nilsson, J. and Stevenson, R. M. and Bennett, A. J. and Shields, A. J. and Burkard, G. and Tartakovskii, A. I. and Skolnick, M. S. and Chekhovich, E. A. Few-second-long correlation times in a quantum dot nuclear spin bath probed by frequency-comb nuclear magnetic resonance spectroscopy *Nature Physics* **12**, 688 (2016).
  - <sup>15</sup> de Lange, G. and van der Sar, T. and Blok, M. and Wang, Z.-H. and Dobrovitski, V. and Hanson, R. Controlling the quantum dynamics of a mesoscopic spin bath in diamond *Scientific Reports* **2**, 382 (2012).
  - <sup>16</sup> Perunovic, V. S. and Hill, C. D. and Hall, L. T. and Hollenberg, L. C. L. A quantum spin-probe molecular microscope *Nature Communications* **7**, 12667 (2016).
  - <sup>17</sup> Waugh, J. S. and Huber, L. M. and Haeberlen, U. Approach to High-Resolution nmr in Solids *Physical Review Letters* **20**, 180 (1968).
  - <sup>18</sup> Rhim, W. K. and Elleman, D. D. and Vaughan, R. W. Enhanced resolution for solid state NMR *Journal of Chemical Physics* **58**, 1772 (1973).
  - <sup>19</sup> Mansfield, P. and Orchard, M. J. and Stalker, D. C. and Richards, K. H. B. Symmetrized Multipulse Nuclear-Magnetic-Resonance Experiments in Solids: Measurement of the Chemical-Shift Shielding Tensor in Some Compounds *Physical Review B* **7**, 90 (1973).
  - <sup>20</sup> Cywinski, L. and Lutchyn, R. M. and Nave, C. P. and Das Sarma, S. How to enhance dephasing time in superconducting qubits *Physical Review B* **77**, 174509 (2008).
  - <sup>21</sup> Álvarez, G. A. and Ajoy, A. and Peng, X. and Suter, D. Performance comparison of dynamical decoupling sequences for a qubit in a rapidly fluctuating spin bath *Physical Review A* **82**, 042306 (2010).
  - <sup>22</sup> Ajoy, A. and Álvarez, G. A. and Suter, D. Optimal pulse spacing for dynamical decoupling in the presence of a purely dephasing spin bath *Physical Review A* **83**, 032303 (2011).
  - <sup>23</sup> Klauder, J. R. and Anderson, P. W. Spectral Diffusion Decay in Spin Resonance Experiments *Physical Review* **125**, 912 (1962).
  - <sup>24</sup> Raitsimring, A. M. and Salikhov, K. M. and Umanskii, B. A. and Tsvetkov, Y. D. Instantaneous diffusion in the electron spin echo of paramagnetic centers stabilized in a solid host *Soviet Physics Solid State* **16**, 492 (1974).

- <sup>25</sup> Tyryshkin, A. M. and Tojo, S. and Morton, J. J. L. and Riemann, H. and Abrosimov, N. V. and Becker, P. and Pohl, H.-J. and Schenkel, T. and Thewalt, M. L. W. and Itoh, K. M. and Lyon, S. A. Electron spin coherence exceeding seconds in high-purity silicon *Nature Materials* **11**, 143 (2012).
- <sup>26</sup> Chekhovich, E. A. and Hopkinson, M. and Skolnick, M. S. and Tartakovskii, A. I. Suppression of nuclear spin bath fluctuations in self-assembled quantum dots induced by inhomogeneous strain *Nature Communications* **6**, 6348 (2015).
- <sup>27</sup> Ladd, T. D. and Maryenko, D. and Yamamoto, Y. and Abe, E. and Itoh, K. M. Coherence time of decoupled nuclear spins in silicon *Physical Review B* **71**, 014401 (2005).
- <sup>28</sup> Maurer, P. C. and Kucsko, G. and Latta, C. and Jiang, L. and Yao, N. Y. and Bennett, S. D. and Pastawski, F. and Hunger, D. and Chisholm, N. and Markham, M. and Twitchen, D. J. and Cirac, J. I. and Lukin, M. D. Room-Temperature Quantum Bit Memory Exceeding One Second *Science* **336**, 1283 (2012).
- <sup>29</sup> Haeberlen, U. and Waugh, J. S. Coherent Averaging Effects in Magnetic Resonance *Physical Review* **175**, 453 (1968).
- <sup>30</sup> Rhim, W. K. and Elleman, D. D. and Vaughan, R. W. Analysis of multiple pulse NMR in solids *Journal of Chemical Physics* **59**, 3740 (1973).
- <sup>31</sup> Burum, D. P. and Rhim, W. K. Analysis of multiple pulse NMR in solids. III *Journal of Chemical Physics* **71**, 944 (1979).
- <sup>32</sup> See Supplemental Material
- <sup>33</sup> Eble, B. and Krebs, O. and Lemaître, A. and Kowalik, K. and Kudelski, A. and Voisin, P. and Urbaszek, B. and Marie, X. and Amand, T. Dynamic nuclear polarization of a single charge-tunable InAs/GaAs quantum dot *Physical Review B* **74**, 081306 (2006).
- <sup>34</sup> Puebla, J. and Chekhovich, E. A. and Hopkinson, M. and Senellart, P. and Lemaitre, A. and Skolnick, M. S. and Tartakovskii, A. I. Dynamic nuclear polarization in InGaAs/GaAs and GaAs/AlGaAs quantum dots under nonresonant ultralow-power optical excitation *Physical Review B* **88**, 045306 (2013).
- <sup>35</sup> Carr, H. Y. and Purcell, E. M. Effects of Diffusion on Free Precession in Nuclear Magnetic Resonance Experiments *Physical Review* **94**, 630 (1954).
- <sup>36</sup> Meiboom, S. and Gill, D. Modified Spin-Echo Method for Measuring Nuclear Relaxation Times *Review of Scientific Instruments* **29**, 688 (1958).
- <sup>37</sup> Suh, B. J. and Borsa, F. and Torgeson, D. R. Use of an Alternating-Phase CPMG Sequence to Avoid Spin-Locking Effects in  $T_2$  Measurements in Solids *Journal of Magnetic Resonance A* **110**, 58 (1994).
- <sup>38</sup> Dementyev, A. E. and Li, D. and MacLean, K. and Barrett, S. E. Anomalies in the NMR of silicon: Unexpected spin echoes in a dilute dipolar solid *Physical Review B* **68**, 153302 (2003).
- <sup>39</sup> Watanabe, S. and Sasaki, S.  $^{29}\text{Si}$  Nuclear-Spin Decoherence Process Directly Observed by Multiple Spin-Echoes for Pure and Carrier-Less Silicon *Japanese Journal of Applied Physics* **42**, L1350 (2003).
- <sup>40</sup> Bar-Gill, N. and Pham, L. M. and Belthangady, C. and Le Sage, D. and Cappellaro, P. and Maze, J. R. and Lukin, M. D. and Yacoby, A. and Walsworth, R. Suppression of spin-bath dynamics for improved

- coherence of multi-spin-qubit systems *Nature Communications* **3**, 858 (2012).
- <sup>41</sup> Ridge, C. D. and O'Donnell, L. F. and Walls, J. D. Long-lived selective spin echoes in dipolar solids under periodic and aperiodic  $\pi$ -pulse trains *Physical Review B* **89**, 024404 (2014).
- <sup>42</sup> Li, D. and Dong, Y. and Ramos, R. G. and Murray, J. D. and MacLean, K. and Dementyev, A. E. and Barrett, S. E. Intrinsic origin of spin echoes in dipolar solids generated by strong  $\pi$  pulses *Physical Review B* **77**, 214306 (2008).
- <sup>43</sup> Franzoni, M. B. and Levstein, P. R. Manifestations of the absence of spin diffusion in multipulse NMR experiments on diluted dipolar solids *Physical Review B* **72**, 235410 (2005).
- <sup>44</sup> Wüst, G. and Munsch, M. and Maier, F. and Kuhlmann, A. V. and Ludwig, A. and Wieck, A. D. and Loss, D. and Poggio, M. and Warburton, R. J. Role of the electron spin in determining the coherence of the nuclear spins in a quantum dot *Nature Nanotechnology* **11**, 885 (2016).
- <sup>45</sup> Moiseev, S. A. and Skrebnev, V. A. Short-cycle pulse sequence for dynamical decoupling of local fields and dipole-dipole interactions *Physical Review A* **91**, 022329 (2015).
- <sup>46</sup> Moiseev, S. A. and Skrebnev, V. A. Symmetric-cycle pulse sequence for dynamical decoupling of local fields and dipole-dipole interactions *Journal of Physics B* **48**, 135503 (2015).
- <sup>47</sup> Khaneja, N. and Reiss, T. and Kehlet, C. and Schulte-Herbrüggen, T. and Glaser, S. J. Optimal control of coupled spin dynamics: design of NMR pulse sequences by gradient ascent algorithms *Journal of Magnetic Resonance* **172**, 296 (2005).

## SUPPLEMENTAL MATERIAL

The supplemental material contains further details on the theoretical tools used to design the CHASE pulse sequences presented in the main text, an analysis of the influence of pulsed spin locking and a discussion of the respective influence of pulse parameters on the performance of these spin control sequences. Finally, the methods used to simulate the spin bath evolution are described with additional results for related pulse sequences from literature.

### Supplemental Note 1. AVERAGE HAMILTONIAN THEORY

Average Hamiltonian theory (AHT) is an established tool for the theoretical characterisation and analysis of pulse sequences for magnetic resonance spin control<sup>S1-S3</sup>. Within certain constraints it allows the time evolution of a given spin Hamiltonian under interaction with a periodic time-dependent external magnetic field to be approximated. We use AHT to determine how well a frequency offset Hamiltonian  $\mathcal{H}_0^z$  and a dipolar coupling term  $\mathcal{H}_d^{zz}$  can be suppressed simultaneously by the CHASE sequences introduced in the main text.

To this end, we consider a nuclear spin ensemble  $I_i$  with spin 1/2. The evolution of the wavefunction  $\psi(t)$  describing the state of the nuclear spin bath is determined by the Schrödinger equation:

$$\partial\psi(t)/\partial t = -(i/\hbar)\mathcal{H}(t)\psi(t) , \quad (1)$$

$$\mathcal{H}(t) = \mathcal{H}_L^z + \mathcal{H}_0^z + \mathcal{H}_d^{zz} + \mathcal{H}_{\text{rf}}(t) , \quad (2)$$

where the Hamiltonian  $\mathcal{H}(t)$  is the sum of the Larmor term  $\hat{H}_L$  describing interaction of the spins with a static magnetic field  $B_z$  along the  $\hat{e}_z$  axis, the offset term  $\mathcal{H}_0^z$  describing static resonance frequency shifts, the dipolar term  $\mathcal{H}_d^{zz}$  describing nuclear-nuclear spin interaction and the radio-frequency (rf) term  $\mathcal{H}_{\text{rf}}(t)$  describing the effect of the oscillating magnetic field inducing nuclear magnetic resonance.

We use transformation into the frame rotating around the direction of the static magnetic field ( $\hat{e}_z$  axis) at the radio-frequency. In this way the effect of the static magnetic field is eliminated ( $\mathcal{H}_L^z = 0$ ) and the oscillating rf field becomes static (see Section 5.5 in<sup>S4</sup>). The explicit time dependence in  $\mathcal{H}_{\text{rf}}(t)$  is then only due to the pulsed nature of the rf field.

The individual terms are explicitly defined as

$$\mathcal{H}_0^z = h \sum_i \Delta\nu_i I_{z,i} , \quad (3)$$

$$\mathcal{H}_d^{zz} = h \sum_{i < j} \nu_{ij} (3I_{z,i} I_{z,j} - \mathbf{I}_i \cdot \mathbf{I}_j) , \quad (4)$$

$$\mathcal{H}_{\text{rf}}(t) = -h\nu_{\text{rf}}(t) \sum_i I_{\varphi,i} . \quad (5)$$

In the studied quantum dots (QDs) the resonance offset term  $\mathcal{H}_0^z$  is dominated by the static quadrupolar frequency shifts ( $\Delta\nu_i$  for the  $i$ -th nuclear spin), although in other systems  $\Delta\nu_i$  could also include different static frequency offsets such as chemical shifts or magnetic field gradients. In addition, we consider a truncated dipolar coupling term  $\mathcal{H}_d^{zz}$  with coupling strength

$$\nu_{ij} = \frac{\mu_0}{4\pi} \frac{\hbar}{2\pi} \frac{\gamma^2}{2} \frac{1 - 3\cos^2\theta}{r^3} , \quad (6)$$

between two spins  $I_i$  and  $I_j$ . Here,  $\mu_0 = 4\pi \cdot 10^{-7} \text{ N/A}^2$  is the magnetic constant,  $\gamma$  is the nuclear gyromagnetic ratio, and  $r$  denotes the length of the vector connecting the two spins, which forms angle  $\theta$  with the  $\hat{e}_z$  axis.

Interaction with resonant rf pulses is described by the time-dependent term  $\mathcal{H}_{\text{rf}}(t)$  where the field amplitude  $\nu_{\text{rf}}(t) = \nu_0$  during a pulse and  $\nu_{\text{rf}}(t) = 0$  otherwise. The spin operator  $I_\varphi$  determines the in-plane rotation axis about which the spin bath precesses under the rf field with a given phase  $\varphi$ :

$$I_\varphi = I_x \cos \varphi + I_y \sin \varphi . \quad (7)$$

Here, we want to study the spin bath evolution under the 'internal' static terms  $\mathcal{H}_{\text{int}} = \mathcal{H}_0^z + \mathcal{H}_d^{zz}$  in the interaction frame of  $\mathcal{H}_{\text{rf}}(t)$ . AHT can give an approximate description of the time evolution after one or more full rf cycles if three conditions are met: (i) The rf Hamiltonian is periodic over the cycle time  $t_c$ , i.e.  $\mathcal{H}_{\text{rf}}(t+t_c) = \mathcal{H}_{\text{rf}}(t)$ . (ii) The net spin rotation after a full rf cycle is a multiple of  $2\pi$ . (iii) Since AHT is a perturbation method in terms of  $t_c/T_2^*$ , the solution only converges quickly if  $|\mathcal{H}_0^z|t_c/\hbar \ll 1$  and  $|\mathcal{H}_d^{zz}|t_c/\hbar \ll 1$ .

We write the total time-evolution operator as

$$\mathcal{U}(t) = \mathcal{T} \exp \left[ -\frac{i}{\hbar} \int_0^t dt' \mathcal{H}(t') \right] = \mathcal{U}_{\text{rf}}(t) \mathcal{U}_{\text{int}}(t) , \quad (8)$$

with Dyson time-ordering operator  $\mathcal{T}$  and

$$\mathcal{U}_{\text{rf}}(t) = \mathcal{T} \exp \left[ -\frac{i}{\hbar} \int_0^t dt' \mathcal{H}_{\text{rf}}(t') \right] , \quad (9)$$

$$\mathcal{U}_{\text{int}}(t) = \mathcal{T} \exp \left[ -\frac{i}{\hbar} \int_0^t dt' \tilde{\mathcal{H}}_{\text{int}}(t') \right] , \quad (10)$$

where we introduced the toggling frame Hamiltonian

$$\tilde{\mathcal{H}}_{\text{int}}(t) = \mathcal{U}_{\text{rf}}^{-1}(t) \mathcal{H}_{\text{int}} \mathcal{U}_{\text{rf}}(t) . \quad (11)$$

While an exact solution for Eq. (10) is generally challenging to find, an approximate description of the spin bath evolution at times  $t = n \cdot t_c$  can be found if conditions (i)-(iii) are fulfilled. In this case, we can apply a Magnus expansion to replace the expression of Eq. (10) by an effective average Hamiltonian  $\bar{\mathcal{H}}$  such that

$$\begin{aligned} \mathcal{U}_{\text{int}}(nt_c) &= \exp \left[ -\frac{i}{\hbar} nt_c \bar{\mathcal{H}} \right] \\ &= \exp \left[ -\frac{i}{\hbar} nt_c \left( \bar{\mathcal{H}}^{(0)} + \bar{\mathcal{H}}^{(1)} + \dots \right) \right] , \end{aligned} \quad (12)$$

with leading order terms

$$\bar{\mathcal{H}}^{(0)} = \frac{1}{t_c} \int_0^{t_c} \tilde{\mathcal{H}}(t) dt , \quad (13)$$

$$\bar{\mathcal{H}}^{(1)} = \frac{-i}{2t_c \hbar} \int_0^{t_c} dt_2 \int_0^{t_2} dt_1 \left[ \tilde{\mathcal{H}}(t_2), \tilde{\mathcal{H}}(t_1) \right] , \quad (14)$$

$$\begin{aligned} \bar{\mathcal{H}}^{(2)} &= \frac{1}{6t_c \hbar^2} \int_0^{t_c} dt_3 \int_0^{t_3} dt_2 \int_0^{t_2} dt_1 \\ &\quad \left( \left[ \tilde{\mathcal{H}}(t_1), \left[ \tilde{\mathcal{H}}(t_2), \tilde{\mathcal{H}}(t_3) \right] \right] \right. \\ &\quad \left. + \left[ \tilde{\mathcal{H}}(t_3), \left[ \tilde{\mathcal{H}}(t_2), \tilde{\mathcal{H}}(t_1) \right] \right] \right) . \end{aligned} \quad (15)$$

The contributions of higher order AHT terms to  $\bar{\mathcal{H}}$  scale as  $t_c^k \Gamma^{k+1}$  for  $\bar{\mathcal{H}}^{(k)}$ , with free decay rate  $\Gamma \propto 1/T_2^*$ . We thus see that in the limit of  $n \rightarrow \infty$  cycles and cycle time  $t_c \rightarrow 0$ , only the zeroth order term  $\bar{\mathcal{H}}^{(0)}$  remains. However, in practice, higher order contributions are rarely negligible, making e.g. longer solid echo sequences such as MREV<sup>S5,S6</sup> and BR-24<sup>S3</sup> more efficient than the shorter WAHUA cycle<sup>S7</sup> in many applications.

We calculate the average Hamiltonian for a spin bath interacting with a given pulse sequence as described by equations (2)-(5) using Mathematica with the freely-available non-commutative algebra package NCAAlgebra<sup>S8</sup>. For the zeroth order average Hamiltonian, we consider finite pulse durations where  $t_\pi$  is the time required for a  $\pi$ -rotation. In this case, the cycle time  $t_c$  is given by the sum of pulse times and pulse spacings  $\tau$ . First and second order terms are only calculated in the limit of infinitely sharp rf pulses  $t_\pi \rightarrow 0$ .

The AHT terms we obtain for the CHASE sequences presented in the main text are listed in Supplemental Table 1. For clarity, we split the  $k$ -th order average Hamiltonian into contributions from the resonance offset ( $\bar{\mathcal{H}}_0^{(k)}$ ) and dipolar Hamiltonian ( $\bar{\mathcal{H}}_d^{(k)}$ ). For higher orders  $k \geq 1$ , we also



Supplemental Table 1. Overview of AHT terms up to second order calculated for the CHASE sequences presented in the main text. Zeroth order terms are calculated assuming finite pulse duration  $t_\pi$  whereas  $t_\pi \rightarrow 0$  is assumed for higher order terms. Unlisted terms  $\bar{\mathcal{H}}_0^{(0),(1),(2)}$ ,  $\bar{\mathcal{H}}_d^{(0),(1),(2)}$ ,  $\bar{\mathcal{H}}_{d0}^{(1),(2)}$  are zero.

AHT term	CHASE-5
$\bar{\mathcal{H}}_0^{(0)}$	$\frac{2t_\pi}{\pi t_c} \mathcal{H}_0^z$
$\bar{\mathcal{H}}_d^{(0)}$	$\frac{it_\pi}{\pi t_c} \{[\mathcal{H}_d^{xx}, I_z] + [\mathcal{H}_d^{yy}, I_x - I_z] - [\mathcal{H}_d^{zz}, I_x]\}$
$\bar{\mathcal{H}}_{d0}^{(1)}$	$\frac{it_c}{18h} [\mathcal{H}_d^{zz} - \mathcal{H}_d^{xx}, \mathcal{H}_0^y]$
$\bar{\mathcal{H}}_d^{(2)}$	$\frac{1}{2} \left(\frac{t_c}{18h}\right)^2 [\mathcal{H}_d^{zz} - \mathcal{H}_d^{xx}, [\mathcal{H}_d^{zz}, \mathcal{H}_d^{yy}]]$
$\bar{\mathcal{H}}_{d0}^{(2)}$	$3 \left(\frac{t_c}{18h}\right)^2 \{[\mathcal{H}_0^y, [\mathcal{H}_0^y, \mathcal{H}_d^{xx} - \mathcal{H}_d^{zz}]] + [\mathcal{H}_d^{zz} - \mathcal{H}_d^{yy}, [\mathcal{H}_0^z, \mathcal{H}_0^y]]\}$
	CHASE-10
$\bar{\mathcal{H}}_{d0}^{(1)}$	$\frac{it_c}{36h} [\mathcal{H}_d^{zz} - \mathcal{H}_d^{xx}, \mathcal{H}_0^y]$
$\bar{\mathcal{H}}_d^{(2)}$	$\frac{1}{2} \left(\frac{t_c}{36h}\right)^2 [\mathcal{H}_d^{zz} - \mathcal{H}_d^{xx}, [\mathcal{H}_d^{zz}, \mathcal{H}_d^{yy}]]$
$\bar{\mathcal{H}}_{d0}^{(2)}$	$3 \left(\frac{t_c}{36h}\right)^2 [\mathcal{H}_0^y, [\mathcal{H}_0^y, \mathcal{H}_d^{xx} - \mathcal{H}_d^{zz}]]$
	CHASE-20
$\bar{\mathcal{H}}_d^{(2)}$	$\frac{1}{2} \left(\frac{t_c}{72h}\right)^2 [\mathcal{H}_d^{zz} - \mathcal{H}_d^{xx}, [\mathcal{H}_d^{zz}, \mathcal{H}_d^{yy}]]$
$\bar{\mathcal{H}}_{d0}^{(2)}$	$3 \left(\frac{t_c}{72h}\right)^2 [\mathcal{H}_0^y, [\mathcal{H}_0^y, \mathcal{H}_d^{xx} - \mathcal{H}_d^{zz}]]$
	CHASE-34
$\bar{\mathcal{H}}_d^{(0)}$	$\frac{it_\pi}{\pi t_c} \{4[\mathcal{H}_d^{xx}, I_y - I_z] + 2[\mathcal{H}_d^{yy}, I_x + 2I_z] - 2[\mathcal{H}_d^{zz}, I_x + 2I_y] + i\pi \mathcal{H}_d^{zz}\}$
$\bar{\mathcal{H}}_{d0}^{(2)}$	$3 \left(\frac{t_c}{108h}\right)^2 \{ \frac{2}{3} [\mathcal{H}_0^y, [\mathcal{H}_0^y, \mathcal{H}_d^{xx} - \mathcal{H}_d^{zz}]] + \frac{2}{3} [\mathcal{H}_d^{zz} - \mathcal{H}_d^{yy}, [\mathcal{H}_0^z, \mathcal{H}_0^y]] - \frac{1}{3} [\mathcal{H}_d^{zz} - \mathcal{H}_d^{xx}, [\mathcal{H}_0^z, \mathcal{H}_0^y]] \}$

include mixed terms ( $\bar{\mathcal{H}}_{d0}^{(k)}$ ). The full  $k$ -th order average Hamiltonian is thus given by

$$\bar{\mathcal{H}}^{(k)} = \bar{\mathcal{H}}_0^{(k)} + \bar{\mathcal{H}}_d^{(k)} + \bar{\mathcal{H}}_{d0}^{(k)} . \quad (16)$$

Only non-vanishing terms are listed, i.e. terms which do not appear in Supplemental Table 1 do not contribute to the total average Hamiltonian.

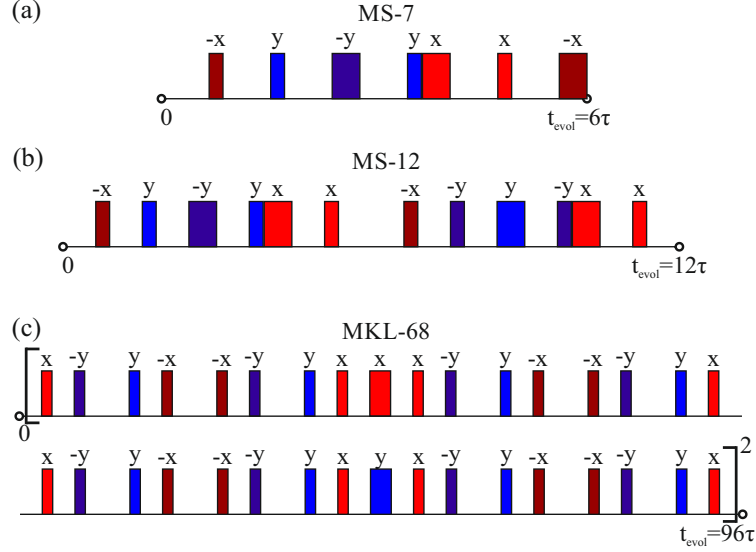
The definition of the additional resonance offset and dipolar coupling Hamiltonians used in Supplemental Table 1 is based on equations (3) and (4), i.e.

$$\mathcal{H}_0^x = h \sum_i \Delta\nu_i I_{x,i} , \quad \mathcal{H}_0^y = h \sum_i \Delta\nu_i I_{y,i} , \quad (17)$$

$$\mathcal{H}_d^{xx} = h \sum_{i < j} \nu_{ij} (3I_{x,i} I_{x,j} - \mathbf{I}_i \cdot \mathbf{I}_j) , \quad \mathcal{H}_d^{yy} = h \sum_{i < j} \nu_{ij} (3I_{y,i} I_{y,j} - \mathbf{I}_i \cdot \mathbf{I}_j) . \quad (18)$$

As discussed in the main text, we see that CHASE-5 has a non-vanishing zeroth order contribution if the pulse duration  $t_\pi$  is non-negligible. In order to suppress spin bath dynamics using cycles of CHASE-5, it is therefore crucial to minimise the ratio  $t_\pi/t_c$ . The subsequent longer sequences are

insensitive to finite pulse durations in zeroth order and leave progressively fewer higher order AHT terms in the  $t_\pi \rightarrow 0$  limit. CHASE-34 forms an exception to this behaviour. While most efficient in suppressing the spin dynamics under ideal conditions, this cycle is also prone to finite pulse effects as the zeroth order dipolar average Hamiltonian contributes to dephasing under realistic experimental conditions.



Supplemental Figure 1. Schematic of alternative pulse sequences from literature for refocusing inhomogeneous and dipolar broadening. Labels are defined as in Fig. 1 of the main text. (a) MS-7 cycle as introduced by Moiseev and Skrebnev in Ref<sup>S9</sup>. (b) MS-12 cycle as introduced by Moiseev and Skrebnev in Ref<sup>S10</sup>. (c) MKL-68 cycle as described and used by Maurer, Kucsko et al. in Ref<sup>S11</sup>.

For comparison, we also calculate the AHT terms of alternative sequences from literature which have been proposed or used with the aim of suppressing both dipolar coupling and frequency offset terms. These results are listed separately in Supplemental Table 2.

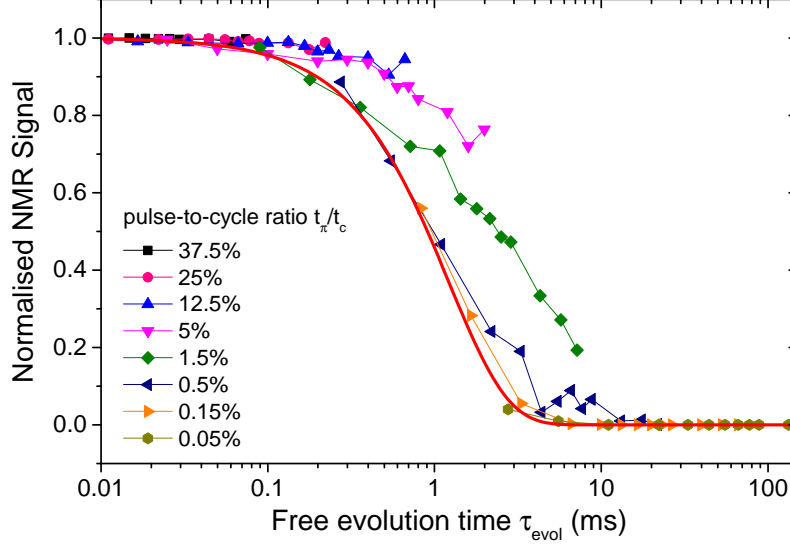
The MS-7 pulse cycle<sup>S9</sup> (Supplemental Fig. 1(b)) yields average Hamiltonians identical to those of CHASE-5 in the short pulse limit. Its extension to MS-12<sup>S10</sup> (Supplemental Fig. 1(c)) removes odd-order AHT terms owing to its symmetry properties. However, unlike the longer CHASE sequences it is not robust against decoherence during a finite pulse duration  $t_\pi$ .

The intuitive approach of alternating MREV cycles with  $\pi$ -pulses (MKL-68, Supplemental Fig. 1(d)) was employed by Maurer, Kucsko et al. to extend nuclear spin coherence times in diamond<sup>S11</sup>. Again, the performance of the cycle is limited under experimental conditions by a non-vanishing zeroth-order term  $\bar{\mathcal{H}}_d^{(0)}$ .

Supplemental Table 2. Overview of AHT terms calculated for other cycles referred to in the main text.

AHT term	MS-7 <sup>S9</sup>
$\bar{\mathcal{H}}_0^{(0)}$	$\frac{2t_\pi}{\pi t_c} \{\mathcal{H}_0^y + \mathcal{H}_0^z\}$
$\bar{\mathcal{H}}_d^{(0)}$	$\frac{it_\pi}{\pi t_c} \{[\mathcal{H}_d^{yy} - \mathcal{H}_d^{zz}, I_x] + \frac{5}{2}i\pi\mathcal{H}_d^{xx} + i\pi\mathcal{H}_d^{yy} + 2i\pi\mathcal{H}_d^{zz}\}$
$\bar{\mathcal{H}}_{d0}^{(1)}$	$\frac{it_c}{18\hbar} [\mathcal{H}_d^{zz} - \mathcal{H}_d^{xx}, \mathcal{H}_0^y]$
$\bar{\mathcal{H}}_d^{(2)}$	$\frac{1}{2} \left(\frac{t_c}{18\hbar}\right)^2 [\mathcal{H}_d^{zz} - \mathcal{H}_d^{xx}, [\mathcal{H}_d^{zz}, \mathcal{H}_d^{yy}]]$
$\bar{\mathcal{H}}_{d0}^{(2)}$	$3 \left(\frac{t_c}{18\hbar}\right)^2 \{[\mathcal{H}_0^y, [\mathcal{H}_0^y, \mathcal{H}_d^{xx} - \mathcal{H}_d^{zz}]] + [\mathcal{H}_d^{zz} - \mathcal{H}_d^{yy}, [\mathcal{H}_0^z, \mathcal{H}_0^y]]\}$
	MS-12 <sup>S10</sup>
$\bar{\mathcal{H}}_d^{(0)}$	$\frac{it_\pi}{\pi t_c} \{[\mathcal{H}_d^{yy} - \mathcal{H}_d^{zz}, 2I_x] + \frac{5}{2}i\pi\mathcal{H}_d^{xx} + \frac{1}{2}i\pi\mathcal{H}_d^{yy} + \frac{5}{2}i\pi\mathcal{H}_d^{zz}\}$
$\bar{\mathcal{H}}_d^{(2)}$	$\frac{1}{2} \left(\frac{t_c}{36\hbar}\right)^2 [\mathcal{H}_d^{zz} - \mathcal{H}_d^{xx}, [\mathcal{H}_d^{zz}, \mathcal{H}_d^{yy}]]$
$\bar{\mathcal{H}}_{d0}^{(2)}$	$3 \left(\frac{t_c}{36\hbar}\right)^2 \{[\mathcal{H}_0^y, [\mathcal{H}_0^y, \mathcal{H}_d^{xx} - \mathcal{H}_d^{zz}]] + [\mathcal{H}_d^{zz} - \mathcal{H}_d^{yy}, [\mathcal{H}_0^z, \mathcal{H}_0^y]]\}$
	MKL-68 <sup>S11</sup>
$\bar{\mathcal{H}}_d^{(0)}$	$\frac{t_\pi}{t_c} \{-2\mathcal{H}_d^{xx} + 6\mathcal{H}_d^{yy} - \mathcal{H}_d^{zz}\}$
$\bar{\mathcal{H}}_d^{(2)}$	$\frac{1}{2} \left(\frac{t_c}{288\hbar}\right)^2 [\mathcal{H}_d^{zz} - \mathcal{H}_d^{xx}, [\mathcal{H}_d^{zz}, \mathcal{H}_d^{yy}]]$
$\bar{\mathcal{H}}_{d0}^{(2)}$	$-3 \left(\frac{t_c}{288\hbar}\right)^2 [\mathcal{H}_0^y, [\mathcal{H}_0^y, \mathcal{H}_d^{xx} - \mathcal{H}_d^{zz}]]$

## Supplemental Note 2. PULSED SPIN LOCKING



Supplemental Figure 2. Dependence of the experimentally measured normalised  $^{71}\text{Ga}$  nuclear spin echo amplitude on the free evolution time  $\tau_{\text{evol}}$  under the phase-alternating CP-X series tested in the main text. Each trace shows data for a fixed pulse-to-cycle ratio  $t_\pi/t_c$  and varying  $\pi$ -pulse number. Values are extracted from exponential decay fits to experimental data as shown in Fig. 2(b) of the main text. The Hahn echo decay fit is shown as a solid red line for comparison.

The extended nuclear spin polarisation decay times we observe in Figs 2(c,d) of the main text under phase-alternated Carr-Purcell sequences (CP-X) are attributed to a form of pulsed spin locking described theoretically by Li et al.<sup>S12</sup> This spin locking mechanism arises due to dipolar evolution during the non-negligible  $\pi$ -pulse duration  $t_\pi$ . As shown by the authors, in this limit application of average Hamiltonian theory yields

$$\bar{\mathcal{H}}^{(0)} = \frac{4t_\pi}{\pi t_c} \mathcal{H}_0^y + \frac{1}{t_c} (4\tau \mathcal{H}_d^{zz} - t_\pi \mathcal{H}_d^{xx}) , \quad (19)$$

for a cycle  $(\tau - \pi_x - 2\tau - \pi_{-x} - \tau)$ . The static term  $\propto \mathcal{H}_0^y$  in equation (19) is subsequently removed by transformation into a second toggling frame where we time-average over a Rabi cycle in its effective field. The twice averaged Hamiltonian is

$$\bar{\bar{\mathcal{H}}}^{(0)} = -\frac{1}{t_c} \left( 2\tau - \frac{t_\pi}{2} \right) \mathcal{H}_d^{yy} . \quad (20)$$

As the initial  $(\pi/2)_x$  pulse of the CP-X sequence prepares the spin bath in the state  $I_y$  which commutes with  $\mathcal{H}_d^{yy}$ , the magnetisation is preserved or ‘locked’ and no spin echo decay is predicted

in zeroth order. Li et al. also examined the cases of fixed-phase CP-X as well as CP-Y with and without phase-alternation and found that, in agreement with our experimental results, no such effect is predicted for the CP-Y sequence tested in the current work<sup>S12</sup>.

Alternative mechanisms leading to prolonged coherence times under CP-X have been suggested by other authors<sup>S13,S14</sup>. However, we can confidently link our experimental observation to the pulsed spin locking mechanism outlined above. A key assumption in the transition to the second toggling frame is that the spin bath evolves slowly under the Hamiltonian  $(4\tau\mathcal{H}_d^{zz} - t_\pi\mathcal{H}_d^{xx})/t_c$  over the relevant timescale set by the Rabi frequency  $\Omega = \frac{4t_\pi\Delta\nu_i}{\pi t_c}$  (c.f. condition (iii) for applicability of AHT in Supplemental Note 1). Hence we expect a strong dependence of the spin locking efficiency on the pulse-to-cycle time ratio  $t_\pi/t_c \in [0, 0.5]$ , where  $t_\pi/t_c \rightarrow 0$  in the limit of infinitely short pulses and  $t_\pi/t_c \rightarrow 0.5$  in the limit of continuous rf excitation.

In Figs 2(a) and 2(b) of the main text we show the nuclear spin polarisation decay as a function of the free evolution time for a fixed number of pulses and varying pulse spacings. In order to verify the dependence of spin locking on the pulse-to-cycle ratio, we now replot this experimental data as a function of the  $\pi$ -pulse number for different fixed pulse-to-cycle ratios. Supplemental Fig. 2 shows that the spin locking efficiency is noticeably reduced for  $t_\pi/t_c \lesssim 10\%$  and the Hahn echo decay (red solid line) is fully restored for  $t_\pi/t_c \lesssim 0.5\%$ .

### Supplemental Note 3. PERFORMANCE BEYOND THE ‘HARD PULSE’ LIMIT

The central transitions (CTs) of the half-integer quadrupolar nuclear spins in a self-assembled QD are typically inhomogeneously broadened to  $\Delta\nu_{\text{inh}} \sim 10 - 40$  kHz by the strain induced electric field gradients<sup>S15</sup>. In order to perform pulse sequences on the full CT experimentally, we need to apply rf pulses which are sufficiently broadband (‘hard’), i.e. have a large enough amplitude to perform the desired  $\pi/2$ - or  $\pi$ -rotation even for spins  $I$  in the tails of the broadened transition spectrum where the rf excitation can have a resonance offset  $\Delta\nu_i \gtrsim 10$  kHz. It is often assumed implicitly that this ‘hard pulse condition’ is fulfilled.

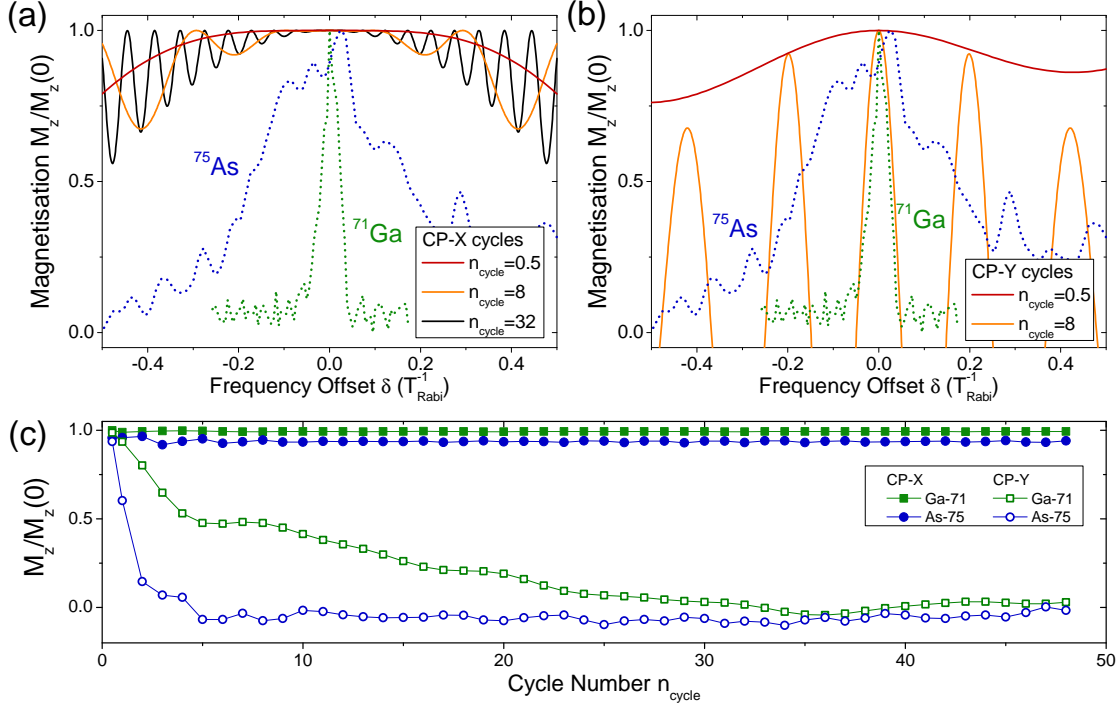
However, while this is readily achievable for small pulse numbers (for a single pulse we require  $T_{\text{Rabi}} \lesssim 2/\Delta\nu_{\text{inh}} \approx 25$   $\mu\text{s}$ ), the hard pulse condition is increasingly difficult to meet for longer sequences. We consider the Bloch equations of motion in the rotating frame of a static magnetic field  $B_z$

$$\partial\vec{M}(t)/\partial t = \vec{\Omega} \times \vec{M} - \vec{\Gamma} \cdot (\vec{M} - \vec{M}_0), \quad (21)$$

describing the evolution of magnetisation  $\vec{M} = \sum_i \gamma I_i$  under an angular velocity vector  $\vec{\Omega} = (\Omega_{\text{rf}} \cos \varphi, \Omega_{\text{rf}} \sin \varphi, 2\pi\Delta\nu_i)^T$  and with relaxation rate  $\vec{\Gamma} = (T_2^{-1}, T_2^{-1}, T_1^{-1})^T$  and equilibrium magnetisation  $\vec{M}_0$ . Here,  $\Omega_{\text{rf}} = 2\pi/T_{\text{Rabi}}$  is the resonant Rabi frequency. We see that even a small resonance offset  $\Delta\nu_i$  results in a slight tilt of  $\vec{\Omega}$  towards the  $\hat{e}_z$  axis. As a consequence, an rf pulse of duration  $T_{\text{Rabi}}$  and carrier phase  $\varphi$  will no longer result in a perfect  $2\pi$ -rotation of the magnetisation  $\vec{M}$  about  $\vec{\Omega}$ . Instead, a small rotation angle error is introduced, which can rapidly lead to non-negligible effects as the errors of subsequent pulses add up. In practice, this is reflected in a loss of NMR signal amplitude after a pulse sequence even in the limit of short free evolution as the contribution of spins with large  $\Delta\nu_i$  to the measured ensemble magnetisation is reduced.

We consider this effect numerically for the  $^{71}\text{Ga}$  and  $^{75}\text{As}$  nuclear spin bath ensembles studied in this work. To quantify the ‘hardness’ (frequency bandwidth) over which a given pulse sequence is stable against resonance offsets, we evaluate the evolution of a magnetisation vector  $\vec{M}$  under the sequence including initialisation and readout  $\pi/2$ -pulses as a function of  $\Delta\nu$ . In order to keep our results as general as possible, we rewrite the resonance offset in terms of the inverse resonant Rabi period as  $\delta = \Delta\nu T_{\text{Rabi}}$ . We can then describe the rescaled rotation axis as  $\hat{e}_{\Omega} = (1+\delta^2)^{-1/2}(\cos \varphi, \sin \varphi, -\delta)^T$ . For added simplicity, our model does not consider any spin relaxation or dephasing (e.g. through dipolar interaction) and we set  $T_1 = T_2 = \infty$ .

Supplemental Figs 3(a,b) show the simulated dependence of the CP-X/Y sequences with alter-

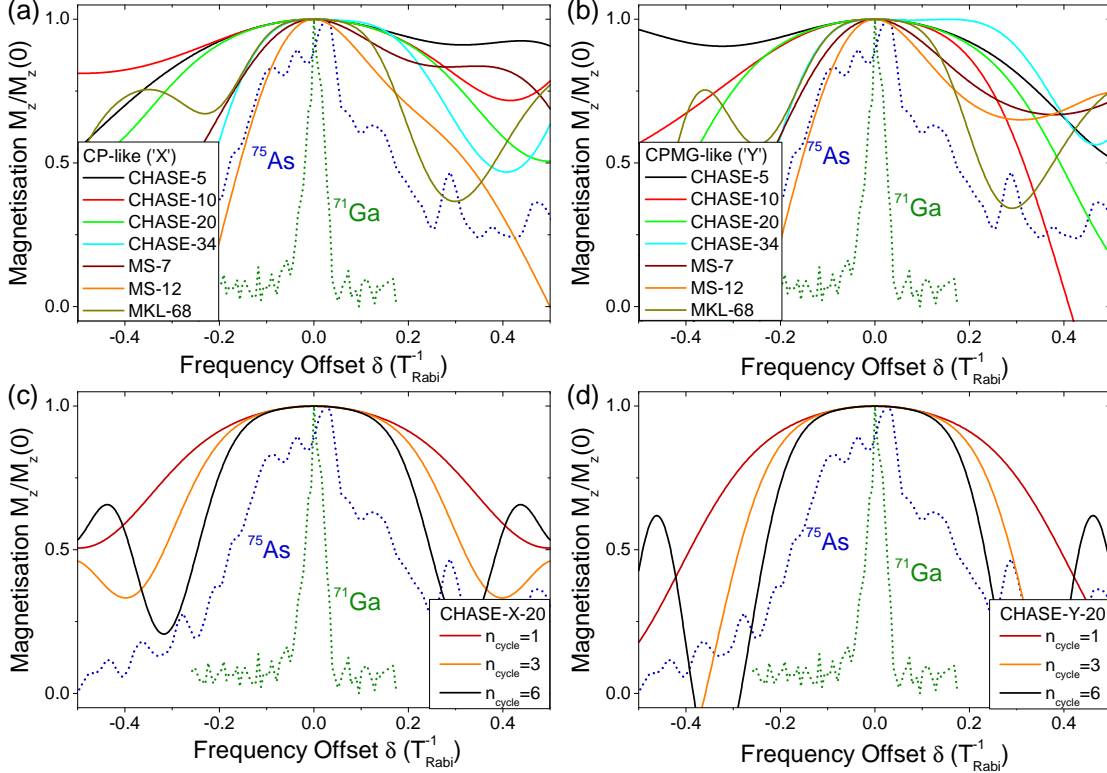


Supplemental Figure 3. (a,b) Normalised magnetisation along the  $\hat{e}_z$  axis after evolution under a series of non-resonant rf pulses as a function of the resonance frequency offset  $\delta$  for (a) CP-X and (b) CP-Y sequences with alternating carrier phase. Solid curves show simulated data for different cycle numbers  $n_{\text{cycle}}$ . Dashed lines show normalised NMR spectra of the  $^{75}\text{As}$  (blue) and  $^{71}\text{Ga}$  (green) central transitions with frequency axes rescaled by  $T_{\text{Rabi}}$ . (c) Weighted average of the normalised magnetisation over the  $^{75}\text{As}$  (circles) and  $^{71}\text{Ga}$  (squares) central transition after a CP-X (solid symbols) or CP-Y (empty symbols) sequence as a function of refocusing cycle number  $n_{\text{cycle}}$ .

ating pulse carrier phase discussed in the main text on the frequency offset  $\delta$ . Solid lines correspond to sets of simulations with different  $\pi$ -pulse numbers. Thus for example, the orange line in Supplemental Fig. 3(a) shows the relative change of the z-component  $M_z/M_z(0)$  of a magnetisation vector  $\vec{M}$  (with  $\vec{M}(0) = (0, 0, 1)^T$ ) after evolution under a CP-X sequence  $(\pi_x/2 - (\pi_x - \pi_{-x})^8 - \pi_x/2)$  for resonance frequency offsets  $-1/2T_{\text{Rabi}} \leq \delta \leq 1/2T_{\text{Rabi}}$ . For comparison, experimental cw NMR spectra of the  $^{71}\text{Ga}$  and  $^{75}\text{As}$  central spin transitions rescaled by the respective shortest Rabi period we could reach experimentally ( $T_{\text{Rabi}}(^{71}\text{Ga}) = 5.6 \mu\text{s}$  and  $T_{\text{Rabi}}(^{75}\text{As}) = 9.8 \mu\text{s}$  at rf power  $P = 200 \text{ W}$ ) are shown as dotted lines.

The desired performance is characterized by  $M_z/M_z(0) \approx 1$  over a wide range of offsets  $\delta$ . In this respect, we note that the CP-X cycle (Supplemental Fig. 3(a)) is very robust against frequency offsets: even at large cycle numbers, the magnetisation vector is largely restored over a large range

of offsets. In practice, this means that we can expect a stable NMR echo amplitude at short evolution times independent of the number of applied  $\pi$ -pulses (as long as additional pulse calibration errors are negligible). This expected behaviour is shown in Supplemental Fig. 3(c): here, we calculate the expected experimental echo amplitude from a weighted average of the normalised final magnetisation over the respective  $^{71}\text{Ga}$  and  $^{75}\text{As}$  NMR spectra for different cycle numbers  $n_{\text{cycle}}$ . In agreement with the experimental data shown in Figs 2(e,f) of the main text, the CP-X signal amplitude (solid symbols) is stable. By contrast, we note in Supplemental Figs 3(b,c) that the ‘bandwidth’ within which the CP-Y sequence can restore the initial magnetisation rapidly narrows with increasing cycle number  $n_{\text{cycle}}$ . Again, this is in agreement with the experimental observation in the main text, where the CP-Y NMR signal amplitude  $\Delta E_{\text{hf}}(\tau_{\text{evol}} = 0)$  rapidly decreases with increasing  $\pi$ -pulse number. Although periodic revivals of the ‘restored’ magnetisation are seen in the orange line of Supplemental Fig. 3(b), these are experimentally compensated by the contribu-



Supplemental Figure 4. Normalised magnetisation along the  $\hat{e}_z$  axis after evolution under a series of non-resonant rf pulses as a function of the resonance frequency offset  $\delta$  for (a) CHASE-X and (b) CHASE-Y sequences and additional cycles from literature. Dashed lines show normalised NMR spectra of the  $^{75}\text{As}$  (blue) and  $^{71}\text{Ga}$  (green) central transitions with frequency axes rescaled by  $T_{\text{Rabi}}$ . (c), (d) Simulated data for CHASE-X/Y-20 with different cycle numbers  $n_{\text{cycle}}$ .



tions of spins at intermediate offsets  $\delta$  where the final magnetisation vector is effectively flipped. This oscillating behaviour arises as the total pulse rotation error adds up to multiple precessions of the magnetisation vector  $\vec{M}$  about  $\hat{e}_\Omega$ .

We run the same simulations for the CHASE sequences introduced in the main text and for the alternative sequences from literature analysed in Supplemental Note 1. The results for the various cycles under ‘X’- and ‘Y’-initialisation pulses are depicted in Supplemental Figs 4(a) and 4(b), respectively. We note that most sequences have a similar ‘hard pulse’ bandwidth under both initialisation pulse conditions. Overall, all of the sequences presented are more stable against resonance offsets than the CP-Y sequence studied in the main text. However, the broadband performance of the CP-X sequence (Supplemental Fig. 3(a)) remains higher than that of any CHASE cycle. This is in qualitative agreement with our experimental results (compare Figs 2(e,f) of the main text).

Additionally, we see that multiple cycles of CHASE-X/Y-20 reduce the offset tolerance to some extent (Supplemental Figs 4(c,d)). This is confirmed experimentally, as the echo amplitude of the spectrally broader  $^{75}\text{As}$  ensemble is noticeably reduced with increasing cycle number in Fig. 2(e) of the main text.

In summary, the reduced NMR signal amplitudes observed in the experiments on the  $^{71}\text{Ga}$  and  $^{75}\text{As}$  CTs presented in the main text can be reproduced qualitatively using a simple Bloch model. We conclude that this is not a fundamental limitation of the various pulse cycles we studied, but can be attributed to ‘soft’ rf pulses which for a given spectral broadening of the spin bath can in principle be avoided by using higher rf excitation powers. Alternatively, more advanced NMR techniques such as composite pulses could be implemented in future experiments to increase the ‘hardness’ of the applied pulses<sup>S16,S17</sup>.

**Supplemental Note 4. NUMERICAL SIMULATION OF THE NUCLEAR SPIN  
EVOLUTION UNDER PULSED RADIOFREQUENCY MANIPULATION**

In this Note we describe the details of the numerical simulation of the quantum mechanical evolution dynamics of the interacting nuclear spin bath.

**A. The model.**

We consider once more the model introduced in Supplemental Note 1, where the evolution of the wavefunction  $\psi(t)$  describing the state of the nuclear spin bath in the rotating frame of an external magnetic field  $B_z$  is determined by:

$$\begin{aligned}\partial\psi(t)/\partial t &= -(i/\hbar)\mathcal{H}(t)\psi(t) , \\ \mathcal{H}(t) &= \mathcal{H}_0^z + \mathcal{H}_d^{zz} + \mathcal{H}_{\text{rf}}(t) .\end{aligned}\tag{22}$$

As before, the Hamiltonian  $\mathcal{H}(t)$  is composed of a term  $\mathcal{H}_0^z$  describing here quadrupolar interaction with electric field gradients, a nuclear dipolar coupling term  $\mathcal{H}_d^{zz}$  and a radio-frequency (rf) term  $\mathcal{H}_{\text{rf}}(t)$ .

We consider half-integer spins  $I$  and simulate evolution only of the  $I_z = \pm 1/2$  subspace corresponding to the NMR experiments on the central transition. The effect of the quadrupolar interaction (more specifically of its second order term) on the  $I_z = \pm 1/2$  manifold is equivalent to an additional magnetic field that changes the Larmor frequency of the  $i$ -th nucleus by  $\Delta\nu_i$ . The quadrupolar term can then be written explicitly as:

$$\mathcal{H}_0^z = 2\pi\hbar \sum_{i=1}^N \Delta\nu_i I_{z,i} ,\tag{23}$$

where the summation goes over all  $N$  nuclei.

We consider the case of high magnetic field (significantly larger than the local dipolar field), so that the nuclear-nuclear interaction is described by the truncated dipole-dipole Hamiltonian:

$$\mathcal{H}_d^{zz} = \frac{\mu_0}{4\pi} \hbar^2 \gamma^2 \sum_{i < j} \frac{x_{i,j}^2 + y_{i,j}^2 - 2z_{i,j}^2}{(x_{i,j}^2 + y_{i,j}^2 + z_{i,j}^2)^{5/2}} \left[ I_{z,i} I_{z,j} - \frac{(I + 1/2)^2}{2} (I_{x,i} I_{x,j} + I_{y,i} I_{y,j}) \right] ,\tag{24}$$

where  $\mu_0 = 4\pi \times 10^{-7}$  N/A<sup>2</sup> is the magnetic constant,  $\gamma$  is the nuclear gyromagnetic ratio,  $(x_{i,j}, y_{i,j}, z_{i,j})$  is the vector connecting spins  $i$  and  $j$  and the summation goes over all pairs of non-identical nuclei. We ignore here any possible contributions from pseudo-dipolar or exchange interactions.

The effect of the rf field is described by:

$$\mathcal{H}_{\text{rf}}(t) = 2\pi\hbar(I + 1/2) \sum_{i=1}^N (\nu_{1,x}(t)I_{x,i} + \nu_{1,y}(t)I_{y,i}) , \quad (25)$$

where parameters  $\nu_{1,x}(t)$  and  $\nu_{1,y}(t)$  characterise the amplitude of the rf magnetic field along the  $x$  and  $y$  axes of the rotating frame respectively. The parameters  $\nu_{1,x}(t)$  and  $\nu_{1,y}(t)$  are piecewise functions of time describing the variation of the rf field amplitude during the pulse sequence.

In the above equations 23, 24 and 25 the operators  $I_x$ ,  $I_y$  and  $I_z$  are spin-1/2 Pauli matrices acting on the effective spin-1/2 subspace of the spin states with spin projections  $I_z = \pm 1/2$ . The factors  $(I + 1/2)$  in equations 24 and 25 (which differ them from equations 3, 4, 5) arise from the matrix elements of the  $I_x$  and  $I_y$  operators of the full spin- $I$  nuclei that are projected on to the  $I_z = \pm 1/2$  subspace. All quantities are in SI units, e.g. frequencies  $\nu$  are in hertz and Hamiltonians are in joules.

The evolution of the nuclear spin magnetisation is calculated by direct propagation of the Schrödinger equation (Eq. 22) using the 6-th order Runge-Kutta method implemented in Mathematica 10.3 and 11.0.1. The Hamiltonian matrices are stored and handled as ‘sparse arrays’ for improved computation efficiency. For a given system of few spins, direct evaluation of Eq. 22 gives an exact evolution of the wavefunction, thus yielding a complete description of the nuclear spin dynamics. The maximum number of spins  $N$  that can be simulated with this direct approach is severely limited by the computation resources, since the memory and the computation time scale approximately as  $\sim N^2$  and  $\sim N^4$  respectively. Thus when performing simulations on a ‘toy’ system with small  $N$ , the choice of the parameters and initial states becomes important for obtaining results that are relevant for systems with much larger  $N$  (such as quantum dots with  $N \geq 10000$ ). The choice of parameters is discussed in the following section.

### B. Model parameters for simulation of the nuclear spin dynamics in quantum dots.

For simulations, nuclear spins are placed at the nodes of the face-centered cubic (fcc) lattice. One nucleus is placed at the origin  $x = y = z = 0$  and the other nuclei are selected from its nearest neighbors – this way the nuclear spin cluster is kept as ‘spherical’ and ‘dense’ as possible which allows approximating the complexity and the magnitude of the dipolar interaction in a 3D lattice. Example clusters with  $N = 6$ ,  $N = 12$  and  $N = 19$  spins are shown in Supplemental Fig. 5(a). The nuclei are taken to be  $^{75}\text{As}$  with gyromagnetic ratio  $\gamma = 2\pi \times 7.29 \times 10^6$  rad/s. The lattice constant of the fcc lattice is taken to be  $a_0 = 0.564786$  nm, corresponding to GaAs at

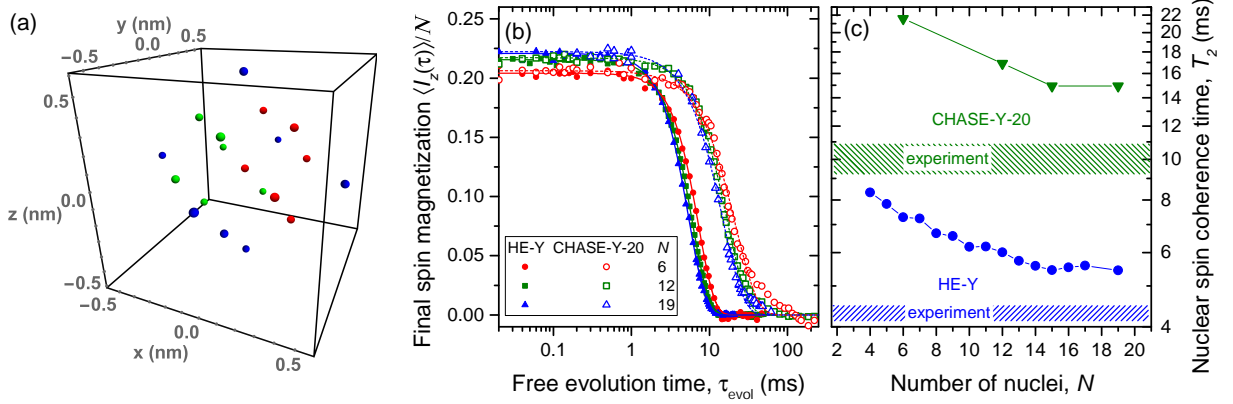
a temperature of  $\sim 4$  K.

Inhomogeneous quadrupolar interaction is introduced by varying the Larmor frequency  $\nu_L$  of each spin (Eq. 23). Firstly, the Larmor frequency of the  $i$ -th spin  $i \in [1, N]$  in the rotating frame is set to be  $\Delta\nu_i = \nu_Q(i - 1/2 - N/2)$ . This equidistant set of  $\Delta\nu_i$  is then rescaled as  $\Delta\nu_i \rightarrow k_1 \times \Delta\nu_i$ , preserving the mean Larmor frequency  $\overline{\Delta\nu_i} = 0$ . The factor  $k_1$  is chosen as an implementation of a uniform random distribution in the range  $[0.77..1.3]$ . At the next step, each frequency  $\Delta\nu_i$  is modified further by adding a random offset  $k_{2,i} \times \nu_Q$  with  $k_{2,i}$  selected randomly for each nucleus from a uniform distribution in the range  $[-0.325, 0.325]$ . The purpose of such a randomisation using parameters  $k_1$  and  $k_{2,i}$  is to eliminate spurious periodic ‘beatings’ in the nuclear spin dynamics arising from the small number of the nuclear spins  $N < 20$  used in the simulations. Such ‘beatings’ are not present in experimental decay curves on real III-V quantum dots where  $N > 10000$ , but similar features are observed for defect spins in dilute nuclear spin baths (e.g. NV centres in diamond), where electron-nuclear hyperfine coupling leads to periodic coherence collapses<sup>S18,S19</sup>. The physical meaning of the randomisation procedure can be seen as follows: The quantum dot can be viewed as built of a large number of clusters, each containing  $N$  spins with a different random distribution of quadrupolar frequencies. The experimentally measured NMR signal is an average over all such clusters, which is simulated by Monte-Carlo averaging over  $k_1$  and  $k_{2,i}$  in the numerical calculations. The step  $\nu_Q$  for the equidistant spacing of Larmor frequencies is chosen to be large compared to the dipolar coupling  $\nu_{ij}$  of any two spins, so that the suppression of dipolar flip-flops arising from quadrupolar interaction (characteristic of self-assembled quantum dots<sup>S20</sup>) can be efficiently simulated. We typically use  $\nu_Q = 2000$  Hz, which is chosen empirically by observing that no change in spin dynamics occurs when  $\nu_Q$  is increased further. The ranges for  $k_1$  and  $k_{2,i}$  are also chosen from trial simulations to be large enough to suppress spurious ‘beatings’ while still small enough to ensure that the minimum difference between any  $\Delta\nu_i$  is large enough to emulate strongly inhomogeneous quadrupolar interaction. When simulating spin dynamics of the nuclei in the absence of quadrupolar effects we use the above procedure with  $\nu_Q$ ,  $k_1$  and  $k_{2,i}$  set to zero.

For initialisation of the nuclear spin system we use the following procedure. Each of the  $N$  nuclear spins is randomly initialised in one of the four single-spin eigen states with  $I_z = -3/2..+3/2$ . The probabilities to find each nucleus in  $I_z = \pm 1/2$  states and  $I_z = \pm 3/2$  are taken to be 60% and 40% respectively. The probabilities for the  $I_z = +1/2$  and  $I_z = -1/2$  states are taken to produce 75% polarisation degree in the  $I_z = \pm 1/2$  subensemble. Such a choice of probabilities corresponds closely to the experimental conditions where optical pumping inducing nuclear spin polarisation

degree of  $\sim 50\%$  is followed by adiabatic radiofrequency sweeps exchanging the populations of  $I_z = \pm 1/2$  and  $I_z = \pm 3/2$  states<sup>S20</sup>. The nuclei in the  $I_z = \pm 3/2$  states are then ignored when simulating the spin dynamics of the  $I_z = \pm 1/2$  states. This is justified since the  $I_z = \pm 3/2$  states have very long correlation times ( $\tau_c \sim 10$  s, Ref.<sup>S21</sup>) and act on the  $I_z = \pm 1/2$  spins simply as a source of quasistatic local magnetic fields which are already taken into account by the inhomogeneous spread of the Larmor frequencies  $\Delta\nu_i$ . This initialisation procedure gives a tensor product random state which is not an eigenstate but where each nucleus is in a single-spin eigenstate with  $I_z = +1/2$  or  $I_z = -1/2$ . In each simulation run (Monte-Carlo sample) the initial function is constructed by repeating the above procedure and creating a linear superposition of 1000 basic random states with random complex weighting coefficients. Such a highly entangled pure state with finite polarisation along  $z$  direction has ‘self-averaging’ properties arising from ‘quantum parallelism’<sup>S22</sup> and allows for faster convergence of the Monte-Carlo simulations.

The typical number of Monte-Carlo samples is 1000. For each Monte-Carlo sample a set of nuclear frequency shifts  $\Delta\nu_i$  is generated (with random parameters  $k_1$  and  $k_{2,i}$ ), the wavefunction is then initialised into a random superposition state as described above. The time evolution of the wavefunction is then calculated numerically from the Schrödinger equation 22 with a Hamiltonian whose time dependence is a piecewise function determined by the rf pulse sequences. The overall time dependence of the nuclear spin polarisation is calculated by averaging over the Monte-Carlo samples. In all simulations the nuclei are first initialised in a state polarised along the  $\hat{e}_z$  axis, then a single  $\pi/2$ -pulse is used to rotate the polarisation into the  $xy$  plane, then a time sequence consisting of rf pulse rotations and free evolution periods is simulated, finally a single  $-\pi/2$ -pulse is used to rotate the magnetisation. All of the studied NMR pulse sequences are cyclic, i.e. in the limit of a short free evolution and ideal rf pulses the magnetisation is returned into its original state along the  $\hat{e}_z$  axis (or into a state with inverted  $z$ -magnetisation for HE-Y, the Meiboom-Gill version of Hahn echo). In simulations we use both ideal (infinitely short, or ‘hard’) and non-ideal (finite duration, or ‘soft’) rectangular rf pulses. The total free evolution time  $\tau_{\text{evol}}$  is varied, and for each value of  $\tau_{\text{evol}}$  the final value of the nuclear magnetisation  $\langle I_z \rangle$  along the  $\hat{e}_z$  axis is computed. The resulting time dependence  $\langle I_z(\tau_{\text{evol}}) \rangle$  reflects the process of nuclear spin decoherence and can be used to derive the coherence time  $T_2$ .



Supplemental Figure 5. (a) Spatial geometry of the  $^{75}\text{As}$  nuclear spin cluster used for numerical simulations. Red balls show a configuration with  $N=6$  spins, red and green with  $N=12$  spins, red, green and blue combined together form a cluster with  $N=19$  spins. (b) Simulated dependence of the final nuclear spin magnetisation  $\langle I_z(\tau_{\text{evol}}) \rangle$  (normalised by the number of spins  $N$ ) on the total free evolution time  $\tau_{\text{evol}}$  under Hahn Echo (HE-Y, solid symbols) and CHASE-Y-20 pulse sequences computed for  $N=6$  spins (circles),  $N=12$  spins (squares), and  $N=19$  spins (triangles). A Meiboom-Gill version of Hahn echo sequence  $(\pi/2_y - \tau_{\text{evol}}/2 - \pi_x - \tau_{\text{evol}}/2 - \pi/2_{-y})$  is used with a  $\pi/2$ -shift between the phases of the  $\pi/2$ - and  $\pi$ -pulses. Lines show the fitting used to derive nuclear spin decoherence times  $T_2$ . (c) Nuclear spin decoherence times  $T_2$  derived from numerical simulations plotted as a function of the number of nuclear spins for Hahn Echo (circles) and CHASE-Y-20 (triangles) pulse sequences. Shaded areas show experimentally measured decoherence times of  $^{75}\text{As}$  spins in a self-assembled quantum dot.

### C. Examples of simulations of the nuclear spin dynamics in quantum dots: dependence on the number of spins $N$ .

We now give several examples of the results obtained from the above described numerical simulation procedure. Several simulated  $\langle I_z(\tau_{\text{evol}}) \rangle$  curves are shown in Supplemental Fig. 5(b) for a Meiboom-Gill version Hahn echo (HE-Y, solid symbols) and CHASE-Y-20 (open symbols) pulse sequences – these are computed for clusters with different numbers of nuclei shown in Supplemental Fig. 5(a) for the case of large inhomogeneous quadrupolar interaction ( $\Delta\nu_i \gg \nu_{ij}$ ). Lines show fitting using compressed exponential functions. For the Hahn echo sequence the decay is close to Gaussian (characterised by compression factor  $\beta \approx 2.0 - 2.1$ ), while for CHASE-Y-20 the best fit is for  $\beta \approx 1.56 - 1.67$ , and some deviation from a mono-exponential decay is observed, especially at small  $N$ .

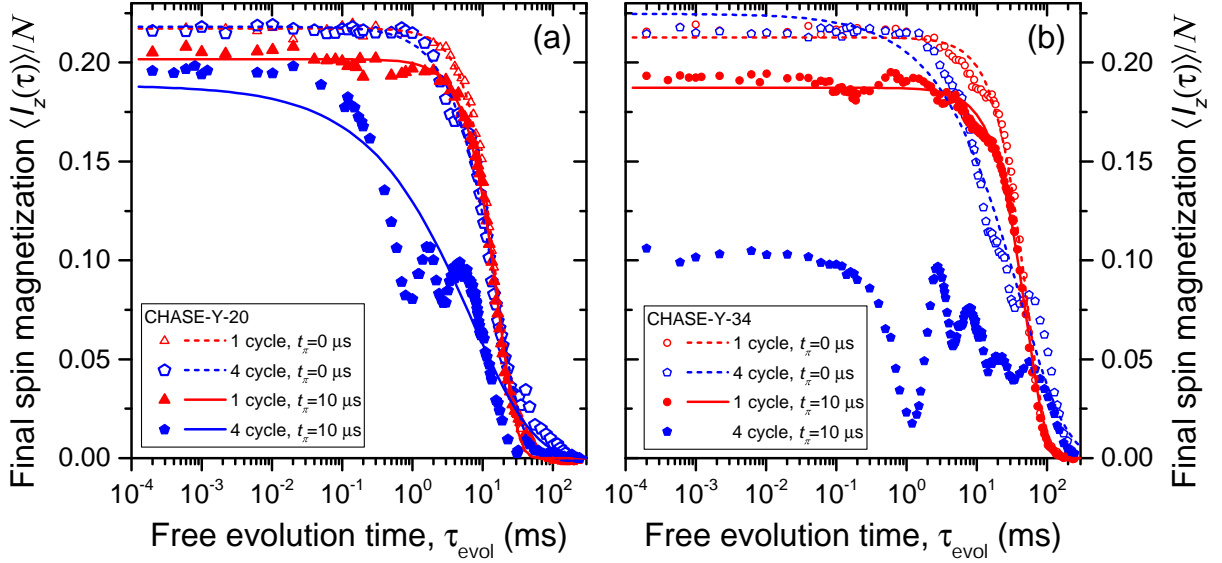
The nuclear spin decoherence times  $T_2$  derived from the fits as in Supplemental Fig. 5(b) are

shown in Supplemental Fig. 5(c) by the symbols and are compared to the experimental values for  $^{75}\text{As}$  spins in self-assembled quantum dots (shaded areas). It can be seen that the number of spins affects the overall timescale of the nuclear spin decoherence – for larger  $N$  the nuclear spin decoherence is faster as the interaction with a larger number of neighbors is taken into account. However, the overall trend in variation of  $T_2$  under different pulse sequences is found to be robust against  $N$ . For example, while the decoherence times  $T_2$  depend on  $N$  as shown in Fig. 5(c), the ratio of the  $T_2$  values under CHASE-Y-20 and Hahn echo sequences is nearly independent of  $N$ , ranging between  $\sim 2.74$  for  $N = 19$  and  $\sim 3.0$  for  $N = 6$  which is in good agreement with the experimental ratio of  $\sim 2.8$ . These test results justify the use of relatively small  $N$  – for most simulations in this work we employ  $N = 12$  giving a good compromise between accuracy and computation time. The fact that the  $T_2$  simulated for  $N = 12$  differs from the experimental  $T_2$  on a system with  $N \sim 10000$  only by  $\sim 50\%$  indicates the robustness of our approach. Thus our simulations (i) give a good quantitative numerical estimate of the absolute  $T_2$  values, and (ii) provide an excellent tool for examining the effect of various pulse sequences on  $T_2$ .

#### **D. Procedure for derivation of the nuclear spin coherence times and echo amplitudes from the results of numerical simulations.**

We now present the raw data of the numerical simulations for the CHASE sequences (Supplemental Fig. 6) and discuss the procedure for analysing the raw data and deriving the spin bath coherence times  $T_2$  and the echo amplitudes  $\langle I_z(\tau_{\text{evol}} = 0) \rangle$  in the limit of short free evolution time  $\tau_{\text{evol}} \rightarrow 0$ . Supplemental Fig. 6(a) shows the simulated spin bath dynamics under CHASE-Y-20. The results are presented for ideal infinitely short (‘hard’) rf control pulses (open symbols) and for the finite (‘soft’) rectangular pulses (solid symbols,  $\pi$ -pulse length of  $t_\pi = 10 \mu\text{s}$ ). The calculations were performed for 1 cycle of the sequence (triangles) and for 4 cycles (pentagons). Lines show best least-squares fits using compressed exponents. These fits are used to derive the spin bath coherence times  $T_2$ . While for 1 cycle the fit is good, for more complex conditions, e.g. 4 cycles and  $t_\pi = 10 \mu\text{s}$ , there is a considerable deviation between numerical experiment and exponential fits – in such cases the  $T_2$  times are still derived from fitting but should be treated as approximate values.

Supplemental Fig. 6(b) shows further results for the spin bath dynamics under the CHASE-Y-34 pulse sequence. Here deviation from the exponential fit is observed for 4 cycles even at  $t_\pi = 0$  while at  $t_\pi = 10 \mu\text{s}$  the oscillations and reduction of the echo amplitude at short free evolution time



Supplemental Figure 6. Simulated dependence of the final nuclear spin magnetisation  $\langle I_z(\tau_{\text{evol}}) \rangle$  (normalised by the number of spins  $N$ ) on the total free evolution time  $\tau_{\text{evol}}$  under CHASE-Y-20 (a) and CHASE-Y-34 (b) pulse sequences computed for  $N = 12$  spins. The results are presented for infinitely short ( $t_\pi = 0$ , open symbols) and finite ( $t_\pi = 10$   $\mu\text{s}$ , solid symbols) control pulses. The calculations were performed for 1 cycle (triangles) and for 4 cycles (pentagons) of the sequence. Lines show best least-squares fits using compressed exponents. In the case of 4 cycles of CHASE-Y-34 with  $t_\pi = 10$   $\mu\text{s}$  the imperfect pulse rotations result in significant loss of transverse nuclear spin magnetisation even at short  $\tau_{\text{evol}}$  – this prohibits unambiguous definition of the coherence time  $T_2$ , thus no fitting results are shown.

$\tau_{\text{evol}} \rightarrow 0$  are particularly pronounced. This requires care when deriving decoherence parameters. Firstly, in our analysis the echo amplitude  $\langle I_z(\tau_{\text{evol}} = 0) \rangle$  is derived not from fitting but rather by taking the average spin magnetisation  $\langle I_z \rangle$  (normalised by the number of nuclei  $N$ ) at short free evolution times  $\tau_{\text{evol}} < 5$   $\mu\text{s}$  – this definition of  $\langle I_z(\tau_{\text{evol}} = 0) \rangle$  is not affected by deviation of the spin decay from the exponential model. Secondly, for any cyclic pulse sequences with ideal ‘hard’ pulses ( $t_\pi = 0$ ) the resulting magnetisation  $\langle I_z(\tau_{\text{evol}} = 0) \rangle$  after the sequence with short free evolution  $\tau_{\text{evol}} \rightarrow 0$  is by definition equal to the initial magnetisation  $\langle I_z(t = 0) \rangle$  before the pulse sequence is applied (in the studied example  $\langle I_z(t = 0) \rangle / N \approx 0.217$ ), while for non-ideal pulses ( $t_\pi > 0$ ) nuclear spin magnetisation at  $\tau_{\text{evol}} \rightarrow 0$  may be lost simply due to the imperfect spin rotations (i.e. due to the ‘soft’ pulse conditions). Such imperfect rotations mean that the spin bath states during free evolution periods of finite duration  $\tau_{\text{evol}} > 0$  deviate from the desired sequence. Under such conditions (e.g.  $t_\pi = 10$   $\mu\text{s}$  in Supplemental Fig. 6) the reduction in  $\langle I_z(\tau_{\text{evol}}) \rangle$  is not related to



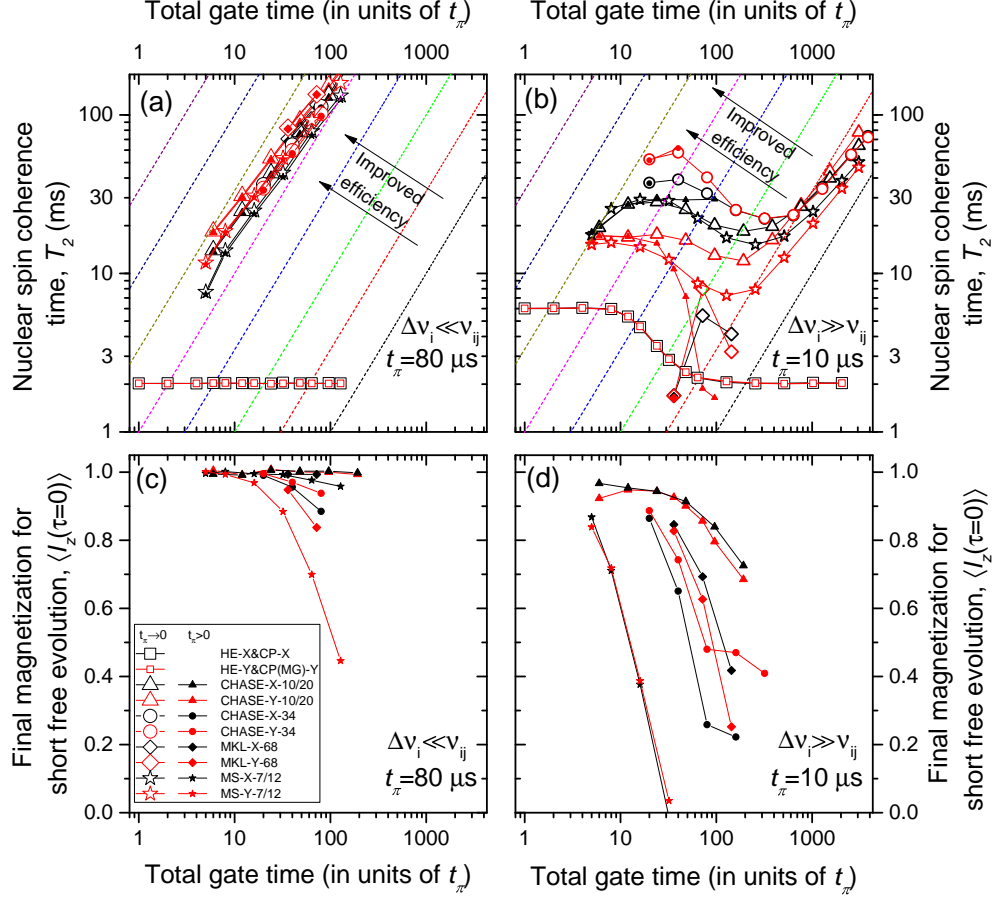
decoherence as such, prohibiting any unambiguous definition for  $T_2$ .

Taking into account the above arguments we establish an approach to the analysis of the numerical results which can be summarised as follows: The echo amplitude  $\langle I_z(\tau_{\text{evol}} = 0) \rangle$  is derived by averaging the  $I_z$  over short free evolution times  $\tau_{\text{evol}} < 5 \mu\text{s}$ . For echo amplitudes  $\langle I_z(\tau_{\text{evol}} = 0) \rangle$  below 70% of the initial magnetisation  $\langle I_z(t = 0) \rangle$  the coherence time  $T_2$  is undefined, while for  $\langle I_z(\tau_{\text{evol}} = 0) \rangle$  above this threshold, the  $T_2$  is derived from fitting with compressed exponential functions. Moreover, in the main text and the subsequent discussion we present echo amplitudes at short free evolution times  $\langle I_z(\tau_{\text{evol}} = 0) \rangle$  normalised by the initial magnetisation  $\langle I_z(t = 0) \rangle$ .

#### **E. Suppression of the nuclear spin fluctuations under various pulse sequences: results of numerical simulations.**

In the main text we present the results of numerical simulations for the pulse sequences used in the experimental work. Simulations are in good agreement with the experiment and confirm robust extension of the nuclear spin coherence time  $T_2$  under CHASE pulse sequences. In this section we present simulated nuclear spin dynamics under alternative pulse sequences reported in the literature and compare their performance to CHASE.

Having discussed in the previous section how echo amplitudes  $\langle I_z(\tau_{\text{evol}} = 0) \rangle$  and coherence times  $T_2$  are derived, we now examine their dependence on the control pulse sequence parameters. The results of the simulations are summarised in Supplemental Fig. 7 for the cases of small inhomogeneous quadrupolar interaction ( $\Delta\nu_i \ll \nu_{ij}$ , panels a, c) and large inhomogeneous quadrupolar interaction ( $\Delta\nu_i \gg \nu_{ij}$ , panels b, d). Three types of sequences are presented: (i) CHASE-10/20 as proposed in this work, (ii) the 7 and 12 pulse sequences proposed theoretically by Moiseev and Skrebnev<sup>S9,S10</sup> and labeled MS-7/12 here, (iii) the sequence consisting of 8 MREV-8 pulse trains interwoven with four phase-refocusing  $\pi$ -pulses used by Maurer, Kucsko et al.<sup>S11</sup> in experiments on NV centers in diamond and labeled MKL-68. The results for Hahn Echo (HE) and Carr-Parcell (CP) sequences are shown as well for a reference. The numbers in the sequence labels stand for the total number of rf control pulses in one cycle. All results in Supplemental Fig. 7 are plotted as a function of the total duration of the control rf pulse sequence (total gate time) in the units of the  $\pi$ -pulse duration  $t_\pi$ . Similar to the way the results are presented in the main text, we combine CHASE-10 with CHASE-20 and MS-7 with MS-12: the points with the shortest total gate time correspond to one cycle of CHASE-10 and MS-7 sequences, while points with larger gate times correspond to integer numbers of repeated cycles of CHASE-20 and MS-12. For each sequence we



Supplemental Figure 7. Results of the nuclear spin decoherence numerical simulations for  $N = 12$  dipolar coupled  $^{75}\text{As}$  nuclear spins under rf pulse control sequences for the case of small  $\Delta\nu_i \ll \Delta\nu_{ij}$  (a,c) and large  $\Delta\nu_i \gg \Delta\nu_{ij}$  (b,d) quadrupolar broadening. Symbols in figures (a) and (b) show the nuclear spin coherence times  $T_2$  for different pulse sequences as a function of the total pulse (gate) time in units of  $t_\pi$ . The plot for each type of sequence is obtained by varying the number of cycle repeats; for Hahn Echo (HE), MS-7 and CHASE-10 we consider only one cycle and combine the data with CP, MS-12 and CHASE-20 respectively. The dashed lines represent constant efficiencies of the pulse sequences, defined as coherence time to gate time ratio. The gate time dependencies of the final magnetisation (echo amplitude) at short free evolution  $\langle I_z(\tau_{\text{evol}} = 0) \rangle$  are shown in (c) and (d), the values are normalised by the magnitude of the initial magnetisation  $\langle I_z(t = 0) \rangle$ . Simulations are carried out for both infinitely short ( $t_\pi = 0$ , open symbols) and finite pulses (solid symbols), where we set  $t_\pi = 80 \mu\text{s}$  for  $\Delta\nu_i \ll \nu_{ij}$  and  $t_\pi = 10 \mu\text{s}$  for  $\Delta\nu_i \gg \nu_{ij}$ . The  $\langle I_z(\tau_{\text{evol}} = 0) \rangle$  values in (c) and (d) are plotted only for  $t_\pi > 0$  since at  $t_\pi = 0$  one has  $\langle I_z(\tau_{\text{evol}} = 0) \rangle = 1$  for any cyclic pulse sequence by definition.

consider two cases: with nuclear magnetisation initialised by a  $\pi/2$ -pulse along the same  $\hat{e}_x$  axis as

the  $\pi$ -pulses of the sequence (‘-X’ sequences) and with initialisation along the  $\hat{e}_y$  axis, orthogonal to that of the  $\pi$  pulses (Meiboom-Gill version, labeled ‘-Y’).

1. *The case of zero inhomogeneous resonance broadening.*

We first examine the case of zero inhomogeneous resonance broadening  $\Delta\nu_i \ll \nu_{ij}$  (negligible quadrupolar effects or chemical shifts) as shown in Supplemental Fig. 7(a),(c). It follows from Supplemental Fig. 7(a) that all three types of sequences can be used to achieve arbitrarily long nuclear spin coherence time: the  $T_2$  increases approximately linearly with the increasing number of sequence repetitions (increasing total gate time). This is largely expected from AHT – when the number of cycles is increased, the cycle duration  $t_c$  is reduced, and the average Hamiltonian converges to its remaining zeroth order term  $\bar{\mathcal{H}}_d^{(0)}$ . As shown in Supplemental Tables 1 and 2, this term vanishes for  $t_\pi = 0$  for all studied sequences. For a given total gate time, the  $T_2$  values are very close for all three types of sequences for initial magnetisation along either  $x$  or  $y$  axes – the difference is less than a factor of 2. However, the performance of the sequences is notably different when non-ideal pulses ( $t_\pi > 0$ ) are considered. For both MKL and MS sequences a pronounced loss of magnetisation  $\langle I_z(\tau_{\text{evol}} = 0) \rangle$  at short free evolution (echo amplitudes) is observed for the Meiboom-Gill (‘Y’) versions of the sequences when the number of cycles is increased (Supplemental Fig. 7(c)) – this means that strong nuclear spin decoherence is induced by the finite ‘soft’ control pulses irrespective of decoherence during free evolution between the pulses. By contrast the CHASE sequences show robust performance for an arbitrary direction of the initial nuclear spin magnetisation for the total gate times of up to  $\sim 200t_\pi$  studied here, thus demonstrating their capability to dynamically ‘freeze’ arbitrary fluctuation of the transverse nuclear magnetisation.

2. *The case of large inhomogeneous resonance broadening.*

The case of large inhomogeneous resonance broadening  $\Delta\nu_i \gg \nu_{ij}$  (e.g. strong quadrupolar effects) is presented in Supplemental Fig. 7(b),(d). We start by examining the coherence times under ideal ‘hard’ control pulses ( $t_\pi = 0$ , open symbols in Supplemental Fig. 7(b)). The MKL sequence exhibits reduced  $T_2$  times, which are even shorter (for 1 cycle) than in the case of simple  $\pi$  pulse trains (Carr-Parcell sequences, CP). This is likely due to the fact that the MKL sequence was not designed to be applied to strongly inhomogeneous spin systems in the first place. By contrast,

all of the CHASE and MS sequences provide enhancement in  $T_2$  compared to Hahn echo and CP and show a similar non-monotonic behaviour on the total gate time which is also presented in Fig. 3(b) of the main text for CHASE-10/20 sequences. For the total gate times up to  $\sim 100t_\pi - 200t_\pi$  the nuclear spin coherence time  $T_2$  is seen to decrease. Such reduction is also observed for the CP sequences and is interpreted to arise from fast rotations of the spins by the rf pulses which lead to an effectively shortened spin lifetime and broadened nuclear spin transitions. Such a broadening can compensate for the energy mismatch between the spins induced by the quadrupolar inhomogeneity and restores the dipolar exchange spin-spin flip-flops. This interpretation is readily confirmed by examining the CP results: for a large number of pulse cycles (with the total gate time  $\gtrsim 100t_\pi$ ) the  $T_2$  of the inhomogeneous ( $\Delta\nu_i \gg \nu_{ij}$ , Supplemental Fig. 7(b)) nuclear spin bath reduces to exactly the value of  $T_2 \approx 2.02$  ms observed for the homogeneous bath ( $\Delta\nu_i \ll \nu_{ij}$ , Supplemental Fig. 7(a)) where dipolar flip-flops are allowed. When the number of CHASE or MS sequence cycles is increased further ( $\gtrsim 500t_\pi$  in Supplemental Fig. 7(b)),  $T_2$  increases steadily, indicating suppression of dipolar interactions and convergence of the average Hamiltonian to zero, similar to the homogeneous case ( $\Delta\nu_i \ll \nu_{ij}$ , Supplemental Fig. 7(a)). The interplay between the opposing effects of the reappearance of the flip-flops and the convergence of the average Hamiltonian depends strongly on the magnitude of the quadrupolar inhomogeneity and rf pulse duration  $t_\pi$ . However, it is possible to establish a qualitative agreement between the experiment and the simulations: for a wide range of the CHASE-10/20 cycle numbers ( $\lesssim 200t_\pi$  in Supplemental Fig. 7(b)),  $T_2$  is nearly constant – this matches the weak dependence of the experimentally measured  $T_2$  on the number of cycles as observed in Figs 2(c,d) of the main text.

We now examine the effect of the finite ‘soft’ pulses ( $t_\pi > 0$ ) under strong inhomogeneous broadening conditions ( $\Delta\nu_i \gg \nu_{ij}$ , solid symbols in Supplemental Figs 7(b),(d)). It follows from Supplemental Fig. 7(d) that the loss of transverse spin polarisation during the control rf pulses (observed as decrease in the initial echo amplitude  $\langle I_z(\tau_{\text{evol}} = 0) \rangle$ ) is most pronounced for the MS sequences – the spin coherence can be maintained well above  $\langle I_z(\tau_{\text{evol}} = 0) \rangle \sim 0.7$  only for one cycle of MS-7. One cycle of MKL-68 with a total gate time of  $36t_\pi$  can preserve the echo amplitude above the 70% threshold but the resulting coherence time  $T_2 < 2$  ms is shorter than for Hahn echo. By contrast, the CHASE sequences demonstrate the best performance in terms of both preserving the echo amplitude  $\langle I_z(\tau_{\text{evol}} = 0) \rangle$  under long rf pulse trains and enhancing the coherence time  $T_2$ . While CHASE-20 can maintain  $\langle I_z(\tau_{\text{evol}} = 0) \rangle > 0.7$  for gate times  $> 100t_\pi$ , the coherence time  $T_2$  decreases abruptly above  $24t_\pi$  in case of the ‘Y’ initialisation pulse. A robust performance in terms of ‘freezing’ of the spin bath fluctuation using finite pulses is obtained for either CHASE-10/20 or

CHASE-34 for the total rf pulse gate times up to  $20 - 24t_\pi$  with CHASE-34 producing a longer coherence time  $T_2$ .

### 3. Analysis and discussion.

In various applications of magnetic resonance it is a common aim to seek for an optimal shape of the rf control field that produces the desired spin manipulation<sup>S23,S24</sup>. It is thus useful to compare the different pulse sequences discussed here by introducing a quantity that characterises their efficiency. To this end we take the ratio of the coherence time  $T_2$  during free evolution and the duration of the rf control pulses required to achieve such  $T_2$  – in other words, the pulse sequence is more efficient if it yields increased  $T_2$  at reduced overhead of spin manipulation via the rf control pulses. The dashed lines in Supplemental Figs 7(a),(b) show constant efficiency levels (given by linear functions with different slopes). It follows from Supplemental Fig. 7(a) that in case of zero inhomogeneous resonance broadening ( $\Delta\nu_i \ll \nu_{ij}$ ) the efficiency is nearly invariant, gradually decreasing with the growing number of sequence cycle repeats. In case of large inhomogeneity ( $\Delta\nu_i \gg \nu_{ij}$ ) the increase in the number of sequence cycle repeats (total gate time) leads to reduction in efficiency due to the re-appearance of the dipolar flip-flops discussed above. Supplemental Fig. 7(b) shows that the best efficiency is achieved for one cycle of either MS-7 or CHASE-10, while for one cycle of CHASE-34 the coherence time  $T_2$  can be extended only with some loss in efficiency. These results indicate that when the dipolar-coupled spin bath is inhomogeneously broadened (Supplemental Fig. 7(b)) its coherence can be extended efficiently only by introducing complex pulse sequences that cancel higher order terms of the averaged spin Hamiltonian – this is different from the case of zero inhomogeneous broadening (Supplemental Fig. 7(a)) where cycles of the basic sequence repeated multiple times efficiently enhance the spin bath coherence.

Further improvements in simultaneous suppression of spectral broadening and dipolar couplings in nuclear spin baths may benefit from techniques beyond AHT. One example of such a technique are composite pulses. We have conducted preliminary numerical simulations with modified CHASE sequences, where each pulse is replaced by a composite broadband BB1 pulse<sup>S25</sup>. However, these pulses give no improvement and in fact result in a slight reduction of the nuclear spin coherence times  $T_2$ , while requiring significantly longer gate times (and hence reduced efficiency). Alternative approaches may involve more sophisticated tools, including numerical optimization algorithms<sup>S26</sup>.

To summarise the results of these numerical simulations, we find that optimal control of the spin

bath coherence is achieved using one cycle of the CHASE-10, CHASE-20, or CHASE-34 sequences as they (i) extend the spin bath coherence time  $T_2$  both under small and large inhomogeneous resonance broadening, (ii) show robust preservation of the spin bath magnetisation even under non-ideal finite duration (‘soft’) control pulses, (iii) effectively ‘freeze’ nuclear spin fluctuations regardless of their direction in the plane perpendicular to the external magnetic field. The simulations for CHASE-34 predict significant improvement of the coherence compared to CHASE-10/20 when applied to an inhomogeneously broadened system – this is confirmed in experiment on nuclear spins in self-assembled quantum dots, although in the experiment the loss of spin bath magnetisation is found to be larger than expected from simulations, most likely due the accumulation of amplitude and/or phase errors of the real rf pulses. Overall, the CHASE sequences developed here provide a well balanced performance and can be used to control spin bath fluctuations both in systems with large inhomogeneous resonance broadening (e.g. quantum dots) and systems with small broadening (e.g. defect spins in diamond) where good tolerance to non-ideal finite pulses is required.

---

\* andreas.waeber@wsi.tum.de

† e.chekhovich@sheffield.ac.uk

- S1. Haeberlen, U. and Waugh, J. S. Coherent Averaging Effects in Magnetic Resonance *Physical Review* **175**, 453 (1968).
- S2. Rhim, W. K. and Elleman, D. D. and Vaughan, R. W. Analysis of multiple pulse NMR in solids *Journal of Chemical Physics* **59**, 3740 (1973).
- S3. Burum, D. P. and Rhim, W. K. Analysis of multiple pulse NMR in solids. III *Journal of Chemical Physics* **71**, 944 (1979).
- S4. Slichter, C. P. Principles of Magnetic Resonance *Springer*, corrected third (1996).
- S5. Rhim, W. K. and Elleman, D. D. and Vaughan, R. W. Enhanced resolution for solid state NMR *Journal of Chemical Physics* **58**, 1772 (1973).
- S6. Mansfield, P. and Orchard, M. J. and Stalker, D. C. and Richards, K. H. B. Symmetrized Multipulse Nuclear-Magnetic-Resonance Experiments in Solids: Measurement of the Chemical-Shift Shielding Tensor in Some Compounds *Physical Review B* **7**, 90 (1973).
- S7. Waugh, J. S. and Huber, L. M. and Haeberlen, U. Approach to High-Resolution nmr in Solids *Physical Review Letters* **20**, 180 (1968).
- S8. Helton, J. W. and de Oliveira, M. C. NCAIgebra <http://math.ucsd.edu/~ncalg/> (2017).
- S9. Moiseev, S. A. and Skrebnev, V. A. Short-cycle pulse sequence for dynamical decoupling of local fields and dipole-dipole interactions *Physical Review A* **91**, 022329 (2015).

- S10. Moiseev, S. A. and Skrebnev, V. A. Symmetric-cycle pulse sequence for dynamical decoupling of local fields and dipole-dipole interactions *Journal of Physics B* **48**, 135503 (2015).
- S11. Maurer, P. C. and Kucsko, G. and Latta, C. and Jiang, L. and Yao, N. Y. and Bennett, S. D. and Pastawski, F. and Hunger, D. and Chisholm, N. and Markham, M. and Twitchen, D. J. and Cirac, J. I. and Lukin, M. D. Room-Temperature Quantum Bit Memory Exceeding One Second *Science* **336**, 1283 (2012).
- S12. Li, D. and Dong, Y. and Ramos, R. G. and Murray, J. D. and MacLean, K. and Dementyev, A. E. and Barrett, S. E. Intrinsic origin of spin echoes in dipolar solids generated by strong  $\pi$  pulses *Physical Review B* **77**, 214306 (2008).
- S13. Franzoni, M. B. and Levstein, P. R. Manifestations of the absence of spin diffusion in multipulse NMR experiments on diluted dipolar solids *Physical Review B* **72**, 235410 (2005).
- S14. Ridge, C. D. and O'Donnell, L. F. and Walls, J. D. Long-lived selective spin echoes in dipolar solids under periodic and aperiodic  $\pi$ -pulse trains *Physical Review B* **89**, 024404 (2014).
- S15. Chekhovich, E. A. and Kavokin, K. V. and Puebla, J. and Krysa, A. B. and Hopkinson, M. and Andreev, A. D. and Sanchez, A. M. and Beanland, R. and Skolnick, M. S. and Tartakovskii, A. I. Structural analysis of strained quantum dots using nuclear magnetic resonance *Nature Nanotechnology* **7**, 646 (2012).
- S16. Levitt, M. H. and Freeman, R. NMR population inversion using a composite pulse *Journal of Magnetic Resonance* **33**, 473 (1979).
- S17. Tycko, R. Broadband Population Inversion *Physical Review Letters* **51**, 775 (1983).
- S18. Mims, W. B. Envelope Modulation in Spin-Echo Experiments *Physical Review B* **5**, 2409 (1972).
- S19. Jelezko, F. and Gaebel, T. and Popa, I. and Gruber, A. and Wrachtrup, J. Observation of Coherent Oscillations in a Single Electron Spin *Physical Review Letters* **92**, 076401 (2004).
- S20. Chekhovich, E. A. and Hopkinson, M. and Skolnick, M. S. and Tartakovskii, A. I. Suppression of nuclear spin bath fluctuations in self-assembled quantum dots induced by inhomogeneous strain *Nature Communications* **6**, 6348 (2015).
- S21. Waeber, A. M. and Hopkinson, M. and Farrer, I. and Ritchie, D. A. and Nilsson, J. and Stevenson, R. M. and Bennett, A. J. and Shields, A. J. and Burkard, G. and Tartakovskii, A. I. and Skolnick, M. S. and Chekhovich, E. A. Few-second-long correlation times in a quantum dot nuclear spin bath probed by frequency-comb nuclear magnetic resonance spectroscopy *Nature Physics* **12**, 688 (2016).
- S22. Schliemann, J. and Khaetskii, A. V. and Loss, D. Spin decay and quantum parallelism *Physical Review B* **66**, 245303 (2002).
- S23. Khaneja, N. and Brockett, R. and Glaser, S. J. Time optimal control in spin systems *Physical Review A* **63**, 032308 (2001).
- S24. Souza, A. M. and Álvarez, G. A. and Suter, D. Robust Dynamical Decoupling for Quantum Computing and Quantum Memory *Physical Review Letters* **106**, 240501 (2011).
- S25. Wimperis, S. Broadband, Narrowband, and Passband Composite Pulses for Use in Advanced NMR

- Experiments *Journal of Magnetic Resonance A* **109**, 221 (1994).
- S26. Khaneja, N. and Reiss, T. and Kehlet, C. and Schulte-Herbrüggen, T. and Glaser, S. J. Optimal control of coupled spin dynamics: design of NMR pulse sequences by gradient ascent algorithms *Journal of Magnetic Resonance* **172**, 296 (2005).